

# The Asymmetry of Galaxies: Physical Morphology for Nearby and High Redshift Galaxies

Christopher J. Conselice, Matthew A. Bershad

Department of Astronomy, University of Wisconsin, Madison, 475 N. Charter St. Madison, WI, 53706-1582  
(chris@astro.wisc.edu, mab@astro.wisc.edu)

Anna Jangren

Department of Astronomy and Astrophysics, Pennsylvania State University, 525 Davey Lab, University Park, PA, 16802 (jangren@astro.psu.edu)

*Subject headings:* galaxies: morphology, evolution; galaxies: parameters: asymmetry,color, concentration

## ABSTRACT

We present a detailed study of rotational asymmetry in galaxies for both morphological and physical diagnostic purposes. An unambiguous method for computing asymmetry is developed, robust for both distant and nearby galaxies. By degrading real galaxy images, we test the reliability of this asymmetry measure over a range of observational conditions, e.g. spatial resolution and signal-to-noise (S/N). Compared to previous methods, this new algorithm avoids the ambiguity associated with choosing a center by using a minimization method, and successfully corrects for variations in S/N. There is, however, a strong relationship between the rotational asymmetry and physical resolution (distance at fixed spatial resolution); objects become more symmetric when less well-resolved.

We further investigate asymmetry as a function of galactic radius and rotation. We find the asymmetry index has a strong radial dependence that differs vastly between Hubble types. As a result, *a meaningful asymmetry index must be specified within a well-defined radius representative of the physical galaxy scale.* We enumerate several viable alternatives, which excludes the use of isophotes. Asymmetry as a function of angle ( $A_\phi$ ) is also a useful indicator of ellipticity and higher-order azimuthal structure. In general, we show the power of asymmetry as a morphological parameter lies in the strong correlation with  $(B - V)$  color for galaxies undergoing normal star formation, spanning all Hubble types from ellipticals to irregular galaxies. Interacting galaxies do not fall on this asymmetry-color “fiducial sequence,” as these galaxies are too asymmetric for their color. We propose to use this fact to distinguish between ‘normal’ galaxies and galaxies undergoing an interaction or merger at high redshift.

## 1. Introduction

### 1.1. Galaxy Morphology

Ever since galaxies were recognized as distinct physical systems, one of the main goals in extragalactic astronomy has been to characterize their forms, or morphology, and to determine how this classification relates to physical properties. This basic taxonomical process is indeed the basis for any observational science. The first attempts at classification were on a subjective level, and began with the work of Curtis (1918), Hubble (1926, 1936), and Sandage (1961). As more images of galaxies became available, the morphological system developed by Hubble was generally adopted by all astronomers, and later refined by van den Bergh (1960a, 1960b) and de Vaucoulers (1959). Other morphological systems were also developed by Morgan (1958) based on the correlation of the physical characteristics of galaxy spectra with the concentration of the light profiles. Yet since the time of Hubble’s 1926 work, the system of morphology for galaxies has changed little. When Hubble developed his original morphological system, his sample consisted of mostly nearby, luminous galaxies, with only 3% “irregular” galaxies. These galaxies were not well incorporated in his sequence, but for his purposes, the morphological system developed was adequate for classifying 97% of his sample.

As deeper galaxy catalogues emerged, however, more and more galaxies fell into the catch-all, “irregular” morphological class. Today, Hubble Space Telescope (HST) imaging reveals that a large fraction of distant galaxies have morphologies that do not fit into the the elliptical - spiral Hubble sequence. The Hubble sequence also fails to be useful when classifying galaxies in clusters, with most galaxies classified as S0 or E – classifications which fail to account of the wide range of cluster galaxy properties (e.g. Koopmann & Kinney 1998). Spectral parameters are often more useful in these cases (e.g. Dressler & Gunn 1992). Today we classify irregular galaxies not simply in a morphological system, but with regard to the physical mechanisms in operation or the salient physical conditions (e.g. starburst galaxies, interacting galaxies, gas-rich and gas-poor). A morphological classification which reflects these physical differences would be a powerful tool for studying the mechanisms driving galaxy evolution. Such studies naturally must include high redshift galaxies. Therefore, a morphological system that encompasses all galaxies, and works sensibly over a wide range in redshift is absolutely essential, but at present does not exist.

Recently, new methods of classifying galaxies have been proposed. One line of effort has been to train artificial neural networks to reproduce the Hubble scheme in an objective way (Burda & Feitzinger 1992, Storrie-Lombardi *et al.* 1992, Serra-Ricart *et al.* 1993, Odewahn 1995, Naim *et al.* 1995, Odewahn *et al.* 1996). Spiekermann’s (1992) approach using fuzzy logic was along this line. The number of galaxy images in modern surveys, such as the “Sloan Digital Sky Survey” will be enormous, and hence such automatable methods of morphological classification are desirable. However, a Hubble classification carries with it the limitations mentioned above; a system that can classify galaxies in a straightforward and quantitative manner that is based on a sound physical and morphological basis would be preferable.

Another approach to galaxy classification has been to develop sets of quantitative measures of the bulk image structures of galaxies. These methods have the potential to either replace, modify, or improve the current Hubble scheme. The new classifications generally rely on a set of photometric and/or spectral properties that are internally correlated, and correspond also with the apparent morphology of galaxies. Morgan’s (1958, 1959) use of central light concentration was the first example of such a classification. Indeed, the use of concentration indices for inferring the morphology of galaxies has continued to improve, and along with surface-brightness and asymmetry has become one of the major tools for classifying both nearby and distant galaxies (e.g. Okamura, Kodaira, & Watanabe 1984; Doi *et al.* 1993; Abraham *et al.*

1994; Jangren *et al.* 1999). A different method – applicable for spirals – has been suggested by Elmegreen & Elmegreen (1982): measures of spiral arm morphology, particularly their patchiness, can be used for classification. Related attempts to classify galaxies have included the use of principle component analysis of photometric structures (Whitmore 1984; Watanabe *et al.* 1985; Han 1995). These systems revealed correlations of physical and morphological features of galaxies, but have not been generally adopted for practical use, and the basic Hubble (1926) system still lives on.

A key element missing from recent work listed above is the connection made by Morgan between image structure and stellar content (i.e. between light concentration, or central surface-brightness, and spectral type). Ironically, in parallel to the above efforts to quantify image structure, there has been considerable effort to develop quantitative methods of spectral classification based on broad-band colors (Bershady 1995) and spectra (Connolly *et al.* 1995, Zaritsky *et al.* 1995, Folkes *et al.* 1996, Bromley *et al.* 1998, Ronen *et al.* 1999). What is needed, then, is to go full circle to where Morgan left off, by tying together the spectral types with the quantitative classification based image structure. Here, we propose that using a measure of asymmetry and color for galaxies is a powerful method towards accomplishing this goal. In an accompanying paper (Jangren *et al.* 1999) we explore the additional parameters of size, surface-brightness and image concentration.

## 1.2. Asymmetry as a Physical Classifier

Symmetry has always been one the most basic features and assumptions of most galaxy morphology systems, but also one of the most overlooked for more detailed study. The earliest galaxy morphology papers by Curtis (1918) and Hubble (1926) described galaxies in terms of their symmetry, in most cases a  $180^\circ$  symmetry. Hubble (1926) describes elliptical and spirals galaxies in their most basic terms as systems “characterized by rotational symmetry about dominating nuclei”. In fact, it is striking how symmetric galaxy systems are, and as we will show, almost always have a minimum asymmetry at a  $180^\circ$  rotation angle.

Models of galaxies often assume that the mass distribution of a galaxy is symmetric. Galaxies are, to first order, dynamically relaxed systems. Understanding how and in what manner the distribution of galaxy light is asymmetric can help reveal dynamical processes in galaxies. For example, galaxies disturbed by interactions or mergers will tend to have large asymmetries. For quite some time there has been considerable effort to characterize the asymmetry in HI gas in spiral galaxies (e.g. Baldwin *et al.* 1980; Richter & Sancisi 1994); attempts to do this in optical light are relatively recent (e.g. Rix & Zaritsky 1995; Kornreich, Haynes, & Lovelace 1998; Rudnick & Rix 1998). While HI-studies benefit directly from kinematic data, optical studies offer complementary information since optical photons predominantly come from stars, which are collisionless, and are believed to trace well the underlying matter distribution in the disk.

The quantitative use of asymmetry as a morphological parameter was used first by Schade *et al.* (1995) as a characterization of distant galaxies observed with the Hubble Space Telescope (HST). Further use of symmetry for galaxies in deep HST images has been carried out by Abraham *et al.* (1996a, 1996b) and van den Bergh *et al.* (1996). These papers, however, use asymmetry only as a crude, type-characterization of distant galaxies in the framework of the Hubble Sequence.

Attempts to characterize asymmetry for nearby galaxies, and its usefulness as a morphological parameter within existing frameworks was first carried out by Conselice (1997; hereafter C97). In C97

it was shown that asymmetry increased with Hubble Type, but with a large spread. Potentially more important was the strong correlation found between color and asymmetry, and a lack of a strong correlation between luminosity and asymmetry for the narrow absolute magnitude of the C97 sample.

In this paper we investigate further the relationship between asymmetry and other physical parameters, such as color and luminosity, and the usefulness of asymmetry as a morphological parameter. From these results, our expectations are that asymmetry can be incorporated as a pillar of a new classification system which better describes and correlates with physical features and parameters than the Hubble sequence.

The paper proceeds as follows. The calibration data set of local galaxies used for this study is described in the next section. In §3, we then compare different methods for computing asymmetry, and propose a new procedure for measuring asymmetry as a robust quantity. This method includes an iterative scheme for finding the center of rotation (§3.3), a noise correction (§3.4), and a well-defined radius of extraction. We demonstrate how asymmetry changes as a function of both the rotation angle used to compute it (§4.1), and as a function of galactic radius (§4.2). We also discuss the correlation between asymmetry and other physical parameters, i.e. the  $(B - V)$  color of a galaxy (§4.3), the Hubble type, and the concentration of light (§4.4). Resolution effects are considered in §5.1. In §4.3 we also discuss the causes of asymmetry, concluding that asymmetries are produced by either star formation in spiral arms, or dynamical effects related to interactions with other galaxies. We show these two causes can be distinguished by examining their position in a color-asymmetry diagram. These results are directly applicable to distant galaxies with resolved structure, such as those in the Hubble Deep Field (HDF).

## 2. Calibration Data Set

The data used in this present study are the full set of 113 galaxies in the Frei et al. (1996) catalog (hereafter referred to as the Frei sample). In contrast, C97 was limited to face-on spirals, or ellipticals from the same sample; inclined systems, irregulars and active galaxies were left out.

### 2.1. Photometry

The current sample under study consists of 82 galaxies imaged in the  $B_J$  and  $R$  bands (Gullixson *et al.* 1995), and 31 in the Gunn  $g,r$ , and  $i$  bands. The scale for the  $B_J$  and  $R$  images is  $1.34''$  per pixel with a field of view of  $7' \times 11'$ ; for the  $g,r$ , and  $i$  images the scale was  $1.19'' \text{ pixel}^{-1}$  with a field of view of  $16' \times 16'$ . The  $g,r$ , and  $i$  images have relatively lower S/N than the  $B_J$  and  $R$  images because of substantially shorter exposures times. In addition to the usual processing (bias subtraction and flat-fielding), Frei *et al.* removed foreground stars. Occasionally, a star that is projected on a bright part of the nucleus was not removed, and causes a false high value for the asymmetry number for those galaxies.

For consistency between the above photometric subsets, we use the  $B - V$  colors listed in the *Third Reference Catalogue of Bright Galaxies* (de Vaucouleurs *et al.* 1991, RC3) for purely photometric purposes. (Structural parameters are computed from the images described above.) The adopted  $B - V$  colors are *observed*, i.e. uncorrected for Galactic and internal extinction, and heliocentric velocity (the  $k$ -correction). These corrections are small and hence have no qualitative impact on the conclusions of this paper. We adopt the distances and  $B$  absolute magnitudes given by Tully (1988). We note, however, that these  $M_B$  include the above corrections. (A more consistent treatment is presented in Jangren *et al.* 1999.) The

adopted values of  $M_B$ ,  $B - V$ , and distance are listed in Tables 1 and 2.

## 2.2. Sample Characteristics

The Frei sample includes Hubble types from early ellipticals and S0s, to late-type spirals, irregulars and galaxies with peculiar features. Several of the galaxies in the sample contain features such as rings and bars. Most of the galaxies in the sample are nearby, with a large portion of the ellipticals coming from the Virgo cluster. All of the galaxies were chosen away from the galactic equator and are generally near the Northern Galactic Cap. However, the Frei sample consists only of bright, high surface brightness galaxies. Hence, we are not considering the large population of LSB or dwarf galaxies that make up the bulk of all galaxies in the universe. It is important to realize that the Frei sample is not likely to be an accurate representation of the entire local galaxy population, but only samples a range of Hubble types for the brightest, nearby galaxies.

For illustrative purposes, in the remainder of this paper we have selected 21 galaxies that are representative examples of total sample of 113 used in this study. These 21 galaxies span of T-types, inclinations and colors. The remaining sample can be viewed at <http://astro.princeton.edu/~frei/galaxy>.

## 3. The Asymmetry Algorithm

The asymmetry  $A_\phi$ , where  $\phi$  is the angle of rotation, is a quantitative parameter based on comparing a source image with its rotated counterpart. In principle  $A_\phi$  is straight-forward and quick to measure in its simplest form. We compare several different methods, including those presented by Abraham *et al.* (1996a; hereafter A96) and C97 in the context of a  $\phi = 180^\circ$  rotation, to determine if they are robust morphological measures over a range of astronomical conditions. On this basis, we develop a more sophisticated approach, ultimately based on the algorithm of A96.

### 3.1. Image Preparation

Before a rotational asymmetry measurement can be made, basic digital image processing must be completed (i.e. bias subtraction, field flattening, fringe correction, cosmic-ray removal, and bad pixel interpolation). In addition, any objects in the galaxy’s image which are not part of the galaxy, such as foreground stars, or foreground and background galaxies must be removed by blanking the contaminated portion of the images, or subtracting the contaminating source. Contaminating sources tend to be at random locations with respect to the primary source, and hence residuals from this decontamination process will add to the asymmetry depending on their amplitude relative to the source brightness. In the case of unresolved contaminating sources, e.g. stars, the removal is straightforward. Foreground and background galaxies are more difficult to remove or exclude both because of their more complex and extended image structure, and because their identification as separate from the primary source can require further information and judgment. This complication becomes particularly important in ultra-deep images such as the HDF, but we do not pursue this further here as it is not an issue for the current study.

In addition to any foreground stellar images, the mean background level for each image must be

carefully subtracted. This will become clear in the next section where we define the specific computational algorithm. A significant non-zero background level can radically alter the measured asymmetry value. After a successful background subtraction and object decontamination, however, it is then possible to perform the asymmetry measurement without further image calibration or processing.

### 3.2. Methods of Computation

The rotational asymmetry measurement procedure consists of (1) defining an image center and “extraction” region; (2) rotating the image about this center by angle  $\phi$ , and (3) performing a comparison of the resultant rotated image with the original image, within the extracted region. This comparison, however, can have several mathematical forms. In published studies (e.g. C97, A96), the comparison is made by subtracting the rotated image from the original, although in principle the product or ratio might be useful. We have found that only subtraction appears to work well, and discuss only this possible algorithm further. The details of the centering, and choice of rotation angle (§3.3 and §4.1 respectively) are critical, but do not depend on the mathematical form of the asymmetry algorithm.

Once the rotated image is subtracted from the original image, we then have a residual image of all asymmetric features of the galaxy. The asymmetry measurement is completed by measuring the amplitude of the pixel values in the residual image, and normalizing this amplitude by a corresponding measure in the original image. Here again, several mathematical possibilities exist.

The method used in C97 consists of summing the square of the pixels in the residual image, and normalizing this value by dividing by the sum of the square of the pixels in the original image. Since the pixel values in the residual image will be, on average, half negative and half positive pixel values, half the above ratio gives the asymmetry number for that galaxy:

$$A_{rms}^2 = \frac{\Sigma(I_o - I_\phi)^2}{2\Sigma I_o^2}$$

where  $I_o$  is the intensity distribution in the original image, and  $I_\phi$  is the intensity distribution in the image rotated by angle  $\phi$ . The sum is over all pixels within a prescribed, matching region of the original and rotated images. We will call this procedure the “RMS” asymmetry method.

Operationally similar is to replace the square by the absolute value, as done by Schade *et al.* (1995) and A96. Instead of using a sum of squares of the original image, a sum of the absolute value is used to normalize the residuals:

$$A_{abs} = \frac{\Sigma|(I_o - I_\phi)|}{2\Sigma|I_o|}$$

Again, the sum is over all pixels within a prescribed, matching region of the original and rotated images. We will call this procedure the “ABS” asymmetry method.

For both methods the lowest possible value for the asymmetry parameter is 0, while the highest is 1. A value of 0 corresponds to a galaxy that is completely symmetric, that is the difference  $(I_o - I_\phi) = 0$  at all points in the difference image formed from subtracting the rotated image from the original image. A values of 1 corresponds to a galaxy that is completely asymmetric such that on average  $|(I_o - I_\phi)| = I_o$ . Values for most galaxies lie between these two extremes (see Tables 1, 2, 3, and 4 for  $\phi = 90^\circ$  and  $180^\circ$ ).

Comparing the above two asymmetry computations for  $\phi = 180^\circ$  rotations, we find that the values for  $A_{abs}$  are similar to the the values found for  $A_{rms}$ , as measured in the red. The  $A_{abs}$  values have slightly

larger asymmetries at high  $A$  as can be seen in Figure 1 from the positive value of  $A_{abs}-A_{rms}$  at large  $A_{rms}$ . As a function of wavelength, the RMS asymmetries show a clear trend towards higher differences in  $A(\text{blue}) - A(\text{red})$  at larger (red) asymmetries, as seen in Figure 2; this can be seen to a lesser extent for the ABS method in Figure 3. (Here, ‘blue’ corresponds either to the  $B$  or  $g$  bands, and ‘red’ corresponds to either  $R$  or  $r$  bands.) The average difference in  $A(\text{blue}) - A(\text{red})$  for the RMS method is 0.015 overall, and 0.05 at  $A(\text{red}) > 0.1$ . The ABS method yields asymmetries that are fairly constant between bands with an average  $A(\text{blue}) - A(\text{red})$  of 0.005 over all asymmetry values.

However, we find the ABS method gives a tighter correlation between asymmetry and color than the RMS method, contrary to our expectations. The RMS method was expected to be a better indicator of star formation since it weights higher the brighter, asymmetric features. The brightness of a star forming region in a galaxy is a function of the density, squared, and hence the RMS method should better trace higher contribution from denser regions of star formation. While either method can be used to get physical information, the better correlation of ABS asymmetries with color lead us to use the ABS method for the remainder of the paper.

### 3.3. Centering Corrections

One of the most crucial aspects of the rotational asymmetry computation is the choice of a center of rotation. Centers that differ by only a small amount (relative to a galaxy’s characteristic size) typically produce substantially different asymmetry values. For example, a change in the center of rotation by just one pixel for the Frei *et al.* sample (roughly 1% of a half-light radius) can change the value of the asymmetry by as much as 50%. However, this becomes less of a problem when the scale of the galaxy becomes smaller, such that as the sampling decreases so does the need for precise centering.

To overcome this centering problem, we define the center of rotation to be the position which yields a minimum value for the  $\phi = 180^\circ$  asymmetry. To find such a center in practice, an initial guess is made for a galaxy’s rotational center. This first step can be automated by choosing the mean, or mode of the light distribution as a reasonable initial guess; our tests indicate that the initial guess does not alter the final asymmetry. In most cases, there is a clear central pixel which is approximately in the center of the galaxy, for example, the brightest pixel in the galaxy. For irregular and edge-on galaxies however, there is not a clear-cut brightest point, or even a well defined center, and it is for these galaxies that this method of minimum center is most effective.

Operationally, after the asymmetry is computed at that initial position, the asymmetry is computed again for centers at the surrounding eight points in a  $3 \times 3$  grid. The distance from the central point to the eight surrounding points can be set at any value. In this work, we use a distance of 0.1 pixels, corresponding to roughly 0.1% of the half-light radius. We use the task ‘rotate’ in IRAF to perform the asymmetry measurements via bi-linear interpolation. If the asymmetry parameter at the center is lower than the asymmetry value at any of the eight surrounding points, then the asymmetry parameter is taken to be the value at the center. The algorithm effectively creates a synthetic grid of asymmetry values arranged by  $x,y$  center positions. If the center pixel does not give the asymmetry minimum, as is usually the case, then the procedure repeats, with the new center the pixel value where the minimum was located. This process continues until a minimum is found for the asymmetry. Once this location is found, we define this to be the ‘asymmetry centroid’ and use that computed asymmetry for the asymmetry parameter of the galaxy.

One possible problem with this method of finding the minimum asymmetry is the existence of local

asymmetry minima. We have tested this by computing the asymmetry parameter over a wide range of centers for a set of 21 representative galaxies from the Frei sample. The second columns of Figures 4, 5, 6, and 7 are pictorial representations of the asymmetries values at all pixel locations about the inner 3x3 arcsec of these 21 galaxies. It can be seen in these images that no significant local minima exist throughout the image. While the detailed shape of these ‘asymmetry planes’ differ from galaxy to galaxy (and indeed, contain considerable information about the light distribution) a well-defined minimum exists in each case. In the presence of sufficient noise, this condition will break down. We characterize this behavior via simulations in the following section.

### 3.4. Noise Corrections

The rotational asymmetry, as defined here, is by its very nature a pixel-by-pixel difference algorithm, and hence can be substantially affected by noise. Clearly this effect must be accounted for if asymmetry is to be a robust classifier. An example of the effects of noise on the asymmetry value of a galaxy is illustrated in Figure 8. The effects of both correlated and uncorrelated noise are relevant. Here, however, we develop a correction for uncorrelated noise and defer handling of correlated noise to a later study on the Hubble Deep Field.

The effects of uncorrelated noise in practice are easy to correct by simultaneously performing the asymmetry measurement on both the source and a neighboring, blank area of the image (see A96). The method for computing the asymmetry of the ‘blank’ area is the same as before, with one exception: there is no normalization by the sum of the original pixels, since in the case of the sky-subtracted background, the sum is zero on average. This procedure is then repeated in a ‘centering’ grid until a minimum of the noise is found, precisely the same way the minimum asymmetry of the object is found. This ‘blank’ asymmetry value is then subtracted from the value measured for the object, thereby correcting statistically for the effects of uncorrelated noise present in the object image. The final formula used to compute the asymmetry can be written as:

$$A_{abs} = \min\left[\frac{\sum|(I_o - I_\phi)|}{\sum|I_o|}\right] - \min\left[\frac{\sum|(B_o - B_\phi)|}{\sum|I_o|}\right],$$

where  $I$  represents the image pixels, and  $B$  represents the blank region (background) pixels. Note that the possible range of asymmetry values now spans from 0 to 2. However, due to the application of the minimization condition, the values are rarely ever greater than 1, and this primarily occurs when  $\phi = 90^\circ$ .

When defining a blank region it is necessary to either use an extraction region the same size as the one used on the galaxy, or more practically, scale the sum of the blank region by the relative size of the object to ‘blank region’ areas. The extraction region used to define the background should be big enough to be representative, but should be small and distant enough from the galaxy so as to not include any diffuse light – and hence gradients – from the sources. Figure 8 shows the differences between the computed asymmetry of a galaxy with added noise and the original asymmetry as a function of S/N. It can be seen from this plot that the asymmetry differences becomes very large at lower S/N.

To test how successful our algorithm of removing noise is at effectively reproducing the correct value for the asymmetry parameter, we artificially degraded the Frei *et al.* galaxy images by adding simulated, random noise. The noise-corrected asymmetry values measured in these images allowed us to assess the systematic behavior with S/N. We compute the S/N as ratio of the signal from the galaxy within the half-light radius to the noise contribution from the sky, source, and detector read-noise within the same aperture. Results of these S/N tests are shown in Figure 9. We use 35 galaxies from our sample which span



all Hubble types and inclinations to perform these simulations. We find that for all these various galaxies, the value of asymmetry parameter found at lower S/N is, on average, still near the values found in the original images.

Below  $S/N \sim 100$ , the noise begins to heavily dominate the asymmetry. In this regime, the rotation center yielding the minimum asymmetry (described in Section 3.3) is determined largely by the noise field. This is compensated in the noise correction since we find the minimum again for the blank field where the background correction is calculated. If we did not re-center on the blank region when finding the background-level asymmetry, this correction would get relatively larger than the galaxy’s asymmetry at successively lower S/N values. As a consequence, the corrected asymmetry would systematically become negative at low S/N values. In our current scheme, we avoid this pit-fall. Even for  $S/N < 100$ , our simulations show that measured asymmetries have error bars that still overlap with the actual value, although the errors are very large. Errors for images with  $S/N > 500$  are typically around 0.02 (rms), while at S/N between 100 and 300 have errors around 0.05 (rms). At  $S/N < 100$ , the error on the asymmetry become very high, i.e. exceeding 0.60 (rms) for  $S/N < 50$ . From Figure 9 however, we conclude that for all galaxies with S/N values  $> 100$  their asymmetries can be computed reliably, which we define to be when the rms errors are less than 0.05.

A feature of our asymmetry algorithm, which comes naturally from the noise corrections, is an ability to estimate an error on the computed, corrected asymmetries. We have tested this via Monte Carlo methods and find that these estimates are accurate.<sup>1</sup>

## 4. Results

The following presentation is based on the results in Tables 1 and 2, which list the asymmetry values and their estimated errors for the 113 galaxies in the Lowell and Palomar sample for  $\phi = 180^\circ$  and  $90^\circ$ , computed within the radius  $r(\eta=0.2)$ , and calculated as described in the previous section with centering and noise corrections. The extraction aperture based on the  $\eta$ -function is described in section §4.2.

### 4.1. Asymmetry as a function of $\phi$

Rotational asymmetry, as we have defined it, has heretofore been explored only in the context of  $180^\circ$  rotation. However, rotation by other angles can potentially yield more physical and morphological information. In particular, the azimuthal variations of galaxy light profiles can be probed, akin to the seminal work of Schweizer (1976a, 1976b). While it is not our intent to pursue such a detailed study here, we do show that other angles of rotation can provide diagnostics which allow us to improve upon the utility of the  $180^\circ$  asymmetry correlation with color.

#### 4.1.1. $180^\circ$ Rotation: flocculent and dynamical asymmetries

The rotation of a galaxy by  $180^\circ$  should yield the minimum rotational asymmetry since most galaxies appear to have a strong azimuthal axi-symmetry. As such,  $A_{180}$  is expected to be sensitive both to either

---

<sup>1</sup>The programs used in this paper to compute the various asymmetries can be obtained by emailing one of the authors.

large scale departures from axi-symmetry (e.g. dynamical disturbances or asymmetric modes), or small scale departures from axi-symmetry in the form of star-forming regions. For normal galaxies, it is the later which is of particular interest.

Both ABS and RMS asymmetry methods clearly show that the  $B_J$  band almost always has a higher asymmetry value than the  $R$  band (Figures 2 and 3). This is consistent with the shorter wavelength  $B_J$  band sampling more sensitively the light from the younger stars which are distributed non-uniformly throughout the galaxy. As seen in C97, the difference between  $A(B)$  and  $A(R)$  increases at higher values of the asymmetry. Jangren *et al.* (1999) also show that the difference between  $A(B)$  and  $A(R)$  increases for galaxies with bluer colors. These trends are a further indication that recent star formation is the cause of asymmetries, and in particular that, for the most part, contributions to the asymmetry of normal galaxies come from blue star forming regions in the arms of spirals or irregular galaxies. We refer to this as ‘floculent’ asymmetry. The vast majority of the sample have ‘floculent’ asymmetries and follow the color-asymmetry sequence as seen in Figure 10.

However, asymmetries can also be caused by dynamical events, such as the interaction or merging of two galaxies. We call the asymmetry from these interactions ‘dynamical asymmetry.’ A dynamical event can warp and extend a galaxy, deviating its structure from the symmetric ‘ground state.’ Dynamical asymmetries add to the floculent asymmetry such that dynamically distorted galaxies have asymmetries which are always higher than asymmetries caused solely from star formation processes. The galaxies in the Frei sample that are in the process of a galaxy interaction/merger are labeled in Figure 10; they are too asymmetric for their colors. We will explore this issue, its relation to other physical features of galaxies, and how to effectively use it for morphological classification in later sections.

#### 4.1.2. $90^\circ$ Rotation: Ellipticity

The asymmetry in a  $90^\circ$  rotation ( $A_{90}$ ) is almost always larger than a  $180^\circ$  rotational asymmetry, as seen in Figure 11. The median ratio  $A_{90}/A_{180}$  for the Frei *et al.* sample is roughly 4, but has a wide range at low  $A_{180}$ . There also is a substantial range in  $A_{90}$  for galaxies spanning all values of  $180^\circ$  asymmetry. We interpret these observations simply to mean that galaxies have a strong  $180^\circ$  symmetry yet a variety of projected shapes, which leads to a wide range of  $90^\circ$  rotational asymmetry.

Indeed,  $A_{90}$  can be used to estimate the ellipticity of the light profile. For most normal galaxies  $A_{90}$  correlates strongly with galaxy axis ratio,  $b/a$ , as seen in Figure 13. This can also be verified by visual inspection of Figures 4-7, which are sorted (for each type) by  $A_{90}$ . There is, however, a small contribution of from flocculence to  $A_{90}$ . This can be seen by plotting the axis ratio instead against the difference of  $A_{90}$  and  $A_{180}$  (Figure 13, bottom panel). A tighter correlation can be seen between  $A_{90}$  and the axis ratio in the bottom panel after  $A_{90}$  has been ‘corrected’ for the flocculent component measured by  $A_{180}$ . To first order  $A_{180}$  and  $A_{90}$  should have comparable amplitude due to flocculence alone. While we tried various mathematical schemes to correct  $A_{90}$  using  $A_{180}$ , simple subtraction worked best. On this basis, we suggest that the quantity  $A_{90} - A_{180}$  can be used in place of directly measured axial ratios, for statistical purposes. This is particularly useful for distorted galaxies without well-ordered, elliptical isophotes; in this case the isophotal measurement of ellipticity is problematic, and  $A_{90}$  may prove a useful substitute or diagnostic via comparison to standard isophotal techniques.

As a result of  $A_{90}$ ’s sensitivity to the global azimuthal shape of the light profile,  $A_{90}$  does not correlate as well with morphological type or color as does  $A_{180}$ . For example, at each T-type, there is a larger scatter

in the values for  $A_{90}$  than for values of  $A_{180}$ .  $A_{90}$  measured in two different wavebands, e.g.  $R$  and  $B$  for example, do correlate strongly (Figure 12, both panels). But while  $A_{90}$  in the  $B_J$  band is a bit more asymmetric, we do not see as strong an increase in the difference between  $A(B)_{90} - A(R)_{90}$  as we do for  $A(B)_{180} - A(R)_{180}$  (cf Figure 3 and the bottom panel of Figure 12). We can infer from these observations that  $A_{90}$  is not particularly sensitive to the flocculent asymmetry due to star-formation that  $A_{180}$  most effectively measures. We do note that the dispersions in  $A(\text{blue})-A(\text{red})$  are about twice as large for  $A_{90}$  than for  $A_{180}$ . This may be attributable simply to the larger  $A_{90}$  values.

It is worth noting that spheroidal systems (ellipticals and S0s) stand out as never having  $A_{90} > 0.70$  – uncharacteristic of the other T-types. We expect all ellipticals, being largely devoid of star-formation, to have  $A_{180}$  values  $\approx 0$  along the entire elliptical sequence from E0 to E7. However, only round elliptical galaxies (E0) would be expected to have zero asymmetry values for any rotation angle  $\phi$ . The more the elliptical deviates from a round shape, the more the value of  $A_\phi$  will change as the angle of rotation  $\phi$  changes. Since a measure of  $A_{90}$  can give an idea of the shape, hence the morphology for elliptical galaxies can also be estimated. There is a slight correlation between the Hubble morphological type index for ellipticals (e.g. E6, where  $6 = 10 * (1 - b/a)$ ), but we do not have enough ellipticals in our sample to say whether  $A_{90}$  is useful for determine the Hubble sub-type for ellipticals. As is always true for determining elliptical sub-type, projection effects are an issue.

It also is interesting to note that there is some scatter in the  $A_{90}$  values even for E0s. Either E0s are not completely round, or they contain a hidden disk structure, as proposed by Kormendy & Bender (1996) to explain the isophotal features of elliptical galaxies.

A final point to note about Figure 11 is the objects with extreme  $90^\circ$  asymmetry values, i.e.  $A_{90} > 0.8$  are almost exclusively edge-on systems. Hence by using both  $A_{180}$  and  $A_{90}$ , these galaxies with high inclinations can be singled out in an automatic process.

#### 4.1.3. Azimuthal Rotation Profiles

To test if other angles are instructive as morphological indicators, we have computed the asymmetry index  $A_\phi$  for rotation angles  $\phi$  from 0 to  $360^\circ$  with  $1^\circ$  increments for the 21 galaxy subset representative of the Frei sample defined in §2. These are displayed in the right-most columns of Figures 4-7. Naim & Lahav (1997) have also considered a variety of rotation angles in the context of attempting to define galaxy ‘peculiarity.’ The treatment here is somewhat more general.

The salient feature of all the asymmetry-rotation angle profiles is the remarkable similarity of the basic shape: the asymmetry profile (which starts at 0 by definition at  $\phi = 0^\circ$ ) rises steeply at first, plateaus near  $90^\circ$ , where there is a maximum, and then descends to a local minimum at  $180^\circ$ . To first order, these profiles are remarkably similar for counter-clockwise rotation from  $0 < \phi < 180$  and clockwise rotation from  $0 > \phi > -180$ . In Figures 4-7, the counter-clockwise and clockwise rotation profiles through  $0 < |\phi| < 180$  are shown as solid and dashed curves respectively. The fact that dashed curves are frequently *not* seen reflects this striking similarity. To second order, these profiles are also remarkably similar even about  $90^\circ$  symmetry points, i.e. the curves from  $0 < \phi < 90$  and  $90 < \phi < 180$  are often indistinguishable except near  $\phi = 0$  and  $\phi = 180$ . The profiles are folded every  $90^\circ$  in Figures 4-7 to illustrate this point. We find, like Kornreich *et al.* (1998) that most galaxies are symmetric in  $\phi$ .

The location of the local minimum of the asymmetry rotation profile at the  $180^\circ$  has some interesting

implications. For example, if a galaxy has a triple arm pattern, or a four arm pattern, this could be reflected in minima at  $120^\circ$  or  $90^\circ$ , respectively. Previous work on this topic found a significant number of galaxies with triple arm patterns, revealed by rotations and subtractions similar to what is presented here (Elmegreen *et al.* 1992). While one might conclude that such symmetries must be rare, it is more likely that they are simply of lower amplitude than the basic axi-symmetry inherent to virtually all galaxies in this sample. This axi-symmetry, coupled with projection, determine the primary features in the rotation profiles as described above.

As previously discussed, one may infer that galaxies are axi-symmetric at 180 rotation angles because they are dynamically relaxed; axi-symmetry is the ‘lowest energy state.’ Perturbations from this ‘ground state’ due to recent dynamical events, however, should be revealed in the details of the asymmetry rotation profiles. Indeed, in detail, there *are* variations in the slope of these profiles at all  $\phi$ . These variations appear to correlate with galaxy type.

For example, there are variations in both the location of the maxima near  $\phi = \pm 90$  and local minima near  $\phi = \pm 180$ . The maxima tend towards smaller  $\phi$  for latter types, qualitatively consistent with the results of Naim and Lahav (1997) for what they describe as increasingly ‘peculiar’ systems. Likewise, there are a variety of slopes at any given value of  $\phi$ , and many cases where there are subtle variations in the basic  $90^\circ$  symmetry of the rotation profiles. Measurements of the steepness of slope at several fiducials (e.g.  $0^\circ$ ,  $30^\circ$ ,  $60^\circ$ , and  $90^\circ$ ) could reveal interesting correlations with other physical parameters. While these differences could be quite illuminating for the physical understanding and classification of these systems, such an analysis is left for future work.

## 4.2. Symmetry as a function of Galactic Radius

The asymmetry index is highly sensitive to the aperture size, as illustrated in the third panel of Figures 4-7. The question is, then: what radius should be used? While in principle any radius can be used, one well-defined alternative is to choose a single radius tied to the physical scale of the galaxy. Clearly whatever choice is made, it must be used *consistently* for comparative purposes. We approached this decision by computing  $A_{180}$  first for a wide variety of different, well-defined radii tied to the metric (physical) scale of each galaxy (as described below). We then determined empirically which asymmetry value correlated best with other physical parameters, such as color.

Traditionally, galaxy radii have been defined using a surface brightness criteria, such as the Holmberg radius at  $\mu_B = 26.5 \text{ mag arcsec}^{-2}$ . These radii, defined to be at the galaxy isophote where the galaxy is just distinguished from the sky on a particular set of photographic plates, are often inadequate, inappropriate, or ill-defined when trying to compare a wider range of galaxy types at various distances. For example, low surface-brightness galaxies pose a particular problem here. The  $(1+z)^{-3}$  surface intensity dimming (detected photons per band-pass), coupled with  $k$ -corrections, further makes the definition of an isophotal radius difficult at best, even for normal galaxies. Evolution only adds to the complication in the isophotal approach; and photometric zero-points are also of concern. In short, isophotal radii, while operationally convenient to measure, are prone to a wide variety of systematics and therefore are among the least robust measures of galaxy radii.

When establishing a characteristic galaxy size, a radius should be used that is independent of the over-all normalization of the surface-brightness distribution, and hence independent of redshift and photometric calibration. Two possible alternative to defining radii,  $\theta$ , are based on (i) the  $\eta$ -function

(Petrosian 1976), and (ii) the curve of growth,  $g(\theta)$ . The latter requires a robust, working definition of a total magnitude. Such schemes have been discussed at length elsewhere (e.g. Bershadsky *et al.* 1994, Bershadsky, Lowenthal & Koo 1998), and here we adopt the protocol developed by Jangren *et al.* (1999), which uses twice the radius where  $\eta = 0.2$  to define the total light.<sup>2</sup> Tables 3 and 4 list the asymmetries computed at the various  $\eta$  and curve of growth radii. Based on these measures, we have determined that the radius where  $\eta = 0.2$  delivers the best correlation with  $(B - V)$  color. Asymmetries computed with the other radii also show a correlation in color. In principle, any radius can be used, as long as it is consistently used when comparing different galaxies. Occasionally, the  $\eta = 0.2$  radius yields extraction regions which extend beyond the image boundaries for the Frei sample. When this occurs, we compute the asymmetry at the largest radius possible.

The trend of asymmetry versus aperture radius is useful to determine where sources of asymmetry in a galaxy are coming from, e.g. different relative amounts of nuclear and disk star-formation, or low-frequency asymmetric structures such as off-center bars and oval disks. It is immediately obvious from inspection of Figures 4-7 that for no galaxy is the asymmetry a constant function of radius. This shows the importance of using a standard radius to compute the asymmetry for a galaxy.

We are able to make a few general observations about the distribution of asymmetric light in a galaxy, which is clearly a function of T-type. Ellipticals and S0s look very similar, with their asymmetry peaking at very low radii, and modestly decreasing outward, and then increasing rapidly at high very large radii (Figure 4). The central peak may be due to structures commonly found in the centers of ellipticals (Lauer *et al.* 1995.) The sharp rise in asymmetry at large radii is not necessarily a physical effect, but is a result of the noise correction in a regime where the noise dominates the signal.

In contrast, spiral galaxies (Figure 5 and 6) show an increase in asymmetry with radius, sometimes with local or global maxima at intermediate radii. For the early disks (Sa-b, Figure 5), the maximum is usually at or near the half-light radii. The late-type disks (Sc-d, Figure 6) have their peak asymmetry values at higher radii, usually beyond the half-light radii. The irregulars (Figure 7) also show a remarkable increase in asymmetry as a function of radius, with the inner parts comparatively symmetric. Maxima in the asymmetry as a function of radius diagrams (Figures 5 and 6) for disk systems are typically at the locations of HII regions or dust lanes in spiral arms.

To summarize the observed trends: as galaxies become systematically later in type, the amplitude of asymmetry increases *and* the increase with radius becomes stronger. That is, the latest type galaxies are pronouncedly more asymmetric in their outer parts than in their inner parts compared to earlier-type galaxies. This characteristic could in principle be an objective method for determining a galaxy’s Hubble type. One physical explanation for this trend of larger radii peaks in asymmetries for later types is the increasing dominance of actively star-forming disks in late-type systems. However, other possibilities include increasing specific star-formation rates with galacto-centric radius (Hodge and Kennicutt 1983; Ferguson *et al.* 1998); the late-time accretion of material in the outer disk with a dynamical-relaxed core (e.g. as proposed by Rix & Zaritsky 1995); or tidal interactions with nearby galaxies. These effects, however, would have to be correlated with morphological type.

A more sensitive probe of the physical cause of these radial trends in asymmetry would be to examine the rotational asymmetry in annuli and to compare the ‘specific asymmetry,’ as measured in these annuli, to

---

<sup>2</sup>We follow Kron’s (1995) suggest to use the inverted form of  $\eta(r) \equiv I(r)/\langle I(r) \rangle$ , which equals one at the center of the galaxy and approaches zero at large galactic radii,  $r$ .

the ‘specific color’ of the annuli. As we have argued above, a significant component of the color-asymmetry correlation is due to what we have termed flocculent asymmetry, i.e. the irregular distribution of HII regions in an otherwise axi-symmetric system. However we have also noted that departures from the color-asymmetry trend for normal galaxies appears to be an indication of larger scale asymmetry – what we refer to as dynamical asymmetry. These statements describe the relation between the integrated asymmetry and color of galaxies. In analogy, departures from the color-asymmetry trend in a given annulus might help disentangle where and when a galaxy’s asymmetry is dominated by star-formation or large-scale dynamical asymmetries. The analysis of Kornreich *et al.* (1998), by excluding the inner portion of the galaxy, achieves this goal. Using rotation instead of a modal analysis, and adding more radial resolution would offer further dimension to this study, and we will pursue this elsewhere.

### 4.3. The Correlation of Color and Asymmetry

The color-symmetry diagram is a powerful tool that can be used for both morphological and physical differentiations of galaxies, and hence can be used as a diagnostic for understanding distant galaxies, and galaxy evolution (C97; Conselice & Bershadsky 1999). The color-asymmetry diagram (Figure 10), when using only the normal face on galaxies presents a tight, linear sequence, as shown in C97. This normal-galaxy sequence represents a lower limit where, for any given asymmetry, there are no galaxies with bluer colors; we refer to this as the ‘fiducial’ galaxy color-asymmetry sequence.

When the entire Frei sample is included (with normal, active, edge-on, irregular and peculiar galaxies), still no galaxies are seen to occupy the symmetric-blue region (bottom left part of Figure 10). This shows that blue galaxies – at least in the Frei *et al.* sample – are asymmetric galaxies. Symmetric blue galaxies may exist, however, at higher redshift (e.g. Schade *et al.* 1995).

To first order, the color-asymmetry diagram of Figure 10 gives a wealth of diagnostic information for classifying galaxies of different morphologies. The elliptical and spirals separate distinctly in this diagram. Ellipticals, denoted as large circles, are always found at the upper left portion of the digram where red and symmetric objects are located. Edge on systems, located by tiny dots, occupy the space to the right of the diagram. The spirals and irregular galaxies are the objects plotted as boxes (early types Sa-b), as stars (later types, Sc-d), and as open circles (irregulars) are always bluer and more asymmetric than the ellipticals. In short, the late type galaxies versus early types can clearly be differentiated in an automatic method via the color-asymmetry diagram.

In addition, the color-asymmetry diagram presents the ability to single out galaxies undergoing an interaction or merger. In Figure 10, we have labeled the galaxies which are most likely undergoing an interaction with another galaxy. These objects stand out as being *too asymmetric for their colors* and therefore, star formation can not be the cause of the asymmetry, as it is for the galaxies on the fiducial sequence. Of the six galaxies listed, only one (NGC 5792) is an early type, the remainder are Sc-d systems. NGC 5792’s high asymmetry can be accounted for in part by the residuals left after subtracting a very bright star near the center. One galaxy, NGC 4088 (Arp 18) has an outer arm receding and an elongated nucleus (Vorontsov-Velyaminov 1977; Dahari 1985) – possible evidence for a recent tidal interaction. NGC 4254 is a Virgo cluster spiral that is thought to have an external driving mechanism (Rauscher 1995) – possibly a result of tidal interactions with the core of the Virgo cluster. These are the only galaxies in the Frei sample that have evidence for interactions, and they all can be distinguished by examining their place in the color-asymmetry diagram. Other galaxies that have similar colors as interacting galaxies, such as the

Magellanic Irregular NGC 4449, fall along the fiducial sequence (Figure 10) as its asymmetry is caused by star formation. When applied to images of distant galaxies, this segregation can be used as an effective tool for disentangling possible evolutionary effects, e.g. the role of mergers and interactions as opposed to star formation.

The edge-on galaxy systems stand out in Figure 10 as objects that are too asymmetric for their colors. However, they generally are not as asymmetric as the interacting galaxies, and have redder colors. Indeed, a large portion of the scatter of the galaxies in the color-asymmetry diagram can be accounted for by this inclination, as demonstrated in Figure 14. Here the color-asymmetry diagram is revisited but with galaxies of higher inclinations labeled with larger symbols. (The four sizes represent quartile bins in the observed  $R$ -band  $A_{90}$  distribution.) The galaxies that contribute to the scatter the most also are the most inclined, almost without exception. As one might infer from the tight correlation in Figure 13, one reaches the same conclusion marking sources according to axis ratio instead of  $A_{90}$ . This raises the possibility that the scatter could be reduced with a hybrid asymmetry-color diagram which included or corrected for inclination.

Since inclination potentially can effect both the apparent asymmetry and color, a first step is to determine how each of these parameters is being affected. That galaxies become redder with increasing inclination is of little doubt, yet the behavior of asymmetry with inclination is less obvious. When we plot the color-asymmetry diagram using colors corrected for extinction (de Vaucouleurs 1991) the scatter is dramatically reduced, as seen in Figure 15. From this exercise one may conclude that the effects of inclination on asymmetry are, in comparison to color, second order.

While inclination-corrected colors yield a stronger asymmetry-color relation, ideally we would like a method of correcting for inclination that is robust over a range of distance. Our concern is that the inclination-corrections of de Vaucouleurs (1991) represents an excellent, but fine-tuned algorithm based on large, normal galaxies, and require an accurate identification of a galaxy’s T type and b/a at a rest-frame isophote comparable to what is used locally. We already have discussed at length the problems of basing measurements on isophotes. Our hope is that  $A_{90}$  may offer a more robust substitute. However, examining correlations of the residuals about the observed color-asymmetry relation with  $A_{90}$ , for example, there is no simple empirical way to correct these residuals. This is obvious from a more careful inspection of Figure 14: while it is true that most of the outliers from the fiducial sequence have large  $A_{90}$ , a good number of galaxies with large  $A_{90}$  also lie in this fiducial sequence. We suspect that more information about type – possibly using light concentration – may allow us to achieve a better inclination correction. To develop this possibility requires a larger training sample and will be explored in a future paper.

#### 4.4. The Correlation of Asymmetry with Other Morphological and Physical Parameters

##### 4.4.1. Asymmetry and Image Concentration

There is also a correlation between asymmetry (A) and the concentration (C) of light for galaxies, as first found by A96, and revisited here in Figure 16 using new measurement algorithms. The concentration index is from Jangren *et al.* (1999), and is defined as the logarithm of the ratio of the radii enclosing 20% and 80% of the light. In principle, this diagram could be used for the same classification purposes as color and asymmetry. It could be argued that asymmetry and image concentration are methodologically superior since, unlike color, measures of both asymmetry and concentration do not require knowledge of the source redshift – at least to first order. However, as discussed by Jangren *et al.* (1999), there are substantial dependencies of these image structural parameters on redshift which must be corrected, thereby mitigating

their putative advantage. Our A-C diagram, which has a tighter correlation than A96, is as tight as A-color. One difference is that the A-C is double valued. Nonetheless, this can be handled with an affine parameter, as A96 has effectively done. An advantage that A-C has over A-color is that the edge-on galaxies do not appear to have a substantially different distribution. This is another indication that A is only weakly affected by inclination.

#### 4.4.2. Asymmetry, T-type, and Luminosity

As was shown in C97, the asymmetry value for a galaxy correlates with T-type. For the larger sample used in this paper, the asymmetry - T-type plot is shown in Figure 17, with a similar result, namely that the Hubble sequence is one of increasing asymmetry, with a substantial scatter.

C97 also showed that asymmetry does not correlate strongly with absolute magnitude, illustrated here in the bottom panel of Figure 18 for the larger sample. One might expect such a correlation since color-luminosity relations are known to exist for all galaxies even in the optical (Huchra 1977, Bershadsky 1995), and color and asymmetry are tightly correlated. However, we note that given the limited dynamic range in luminosity of this sample, the lack of a strong correlation between asymmetry and luminosity is not surprising. For example, the color-luminosity correlation exhibited by this sample is paltry for this reason, as illustrated in Figure 18a.

When we test the relationship between the asymmetry parameters and the van den Bergh luminosity classification (van den Bergh 1960a, 1960b) for the subsample with known van den Bergh luminosity types, we again do not see a correlation between these two morphological parameters. This suggests that asymmetry is a perpendicular morphological parameter to the luminosity class of a galaxy. A detailed system of morphology using the T-type, asymmetry and luminosity class of a galaxy is possible, and will be the subject of a separate paper.

## 5. Application to Distant Galaxies

In §3.4 we established that asymmetry can be well-measured for  $S/N \geq 100$  (within the half-light radius). Here we determine the other most relevant observational parameter: the required spatial resolution for accurate asymmetry measurements. For this purpose, we define  $\epsilon$  as the ratio of the angular diameter subtending  $0.5 h_{75}^{-1}$  kpc at a given distance ( $\theta_{0.5kpc}$ , where  $h_{75}^{-1} = H_0 / 75 \text{ km s}^{-1} \text{ Mpc}^{-1}$ ) to the angular resolution of the image ( $\theta_{res}$ ):

$$\epsilon \equiv \frac{\theta_{0.5kpc}}{\theta_{res}}.$$

The choice of numerator stems from the results of our simulations, which, as we will discuss, show the asymmetry parameter was found to be recoverable when the resolution element was greater than  $0.5 h_{75}^{-1}$  kpc. Hence  $\epsilon$  provides an index of the resolving power of a telescope relevant to the measurement of a galaxy's asymmetry.

For subjective morphological classifications, such as the classical Hubble scheme, as one might expect that as long as a galaxy's large scale structure, (e.g. the bulge and disk components) can be resolved, at least a rudimentary classification can be given. For large galaxies, one might estimate that  $\sim 1$  kpc physical resolution is marginally adequate, i.e.  $\epsilon \sim 0.5$ . This resolution is afforded by HST essentially at all redshifts. However, since the appearance of the spiral arms and the flocculence of the disk is important in the Hubble



classification, higher spatial resolution ( $\epsilon \geq 1$ ) is required to make classifications comparable to what is done for nearby galaxies even from ground-based images. Nonetheless, the Hubble scheme has been used to classify distant galaxies as seen in moderate to deep Hubble Space Telescope images (van den Bergh *et al.* 1996), and has been automated using neural networks (e.g. Odewahn *et al.* 1996).

Since a critical component of asymmetry in normal galaxies also is due to ‘floculence,’ then there could be substantial systematics of the observed asymmetry with resolution (distance). In C97, a slight distance effect was seen: the value of the asymmetry parameter (A) was found to decrease very slightly with increasing distance, i.e. the sources appeared to become more symmetric. We find a similar type of relationship using the entire Frei sample, where galaxies on average become more symmetric at higher distances. Mitigating this effect is that the most distant sources in our sample tend to be red and hence have lower intrinsic asymmetry.

To determine the importance of image resolution on the measured asymmetry, we simulated the appearance of the Frei *et al.* galaxy sample, as they would be observed at large distances with, e.g., HST. The simulations are simple in that we considered only the change in apparent size relative to a fixed apparent pixel size. The effects of image blur and redshift (i.e. change in observed portion of the galaxy rest-frame spectrum) were ignored. In other words, we assume here that the point-spread-function (PSF) aberrations are small compared to the pixel size, and that the observed band-pass is shifted with redshift, respectively. Both of these assumptions are reasonable for substantial data sets combining multi-band images using the HST Wide-Field Camera-2.

The sources in the simulated ‘degraded’ images had their asymmetry computed by the same method described in Section 3. The centering algorithm is particularly important here. For less well-resolved sources the relative error in selection of an image can be large. We observed that the mean and mode of the light distribution changed significantly at the pixel level as galaxy’s image was sampled more coarsely, even though the original images of most galaxies had a visually well-defined center.

However, even using our routines which find the minimum asymmetry, we find that almost all galaxies decrease in their asymmetry value when artificially degraded, as shown in Figure 19. Interestingly, we find that the most symmetric galaxies (ellipticals) have asymmetries that initially *increase* at coarser sampling redshifts, an effect also noticed by Wu, Faber & Lauer (1997). Recall that the higher the value of  $\epsilon$ , the better a galaxy is spatially resolved and sampled. As  $\epsilon$  decreases, so too does the asymmetry parameter. However, while the asymmetry parameter does decrease in Figure 19, the  $\epsilon$  values change by a factor of twenty; for  $\epsilon > 1$ , the measured asymmetries remain close to the high- $\epsilon$  value.

Fortunately, the angular size of a galaxy changes little beyond  $z \sim 0.7$  for a wide range of cosmologies. At  $z = 1.25$ , a galaxy observed in the HDF, where  $\theta_{res} \sim 0.045$ , will have  $\epsilon \sim 1.3$  ( $q_0 = 0.5$ ,  $\Lambda = 0$ ), and greater at higher and lower redshifts for this cosmology. In comparison, a typical Frei *et al.* sample galaxy has a size of about  $4'$ , with a pixel size of  $1.35''$ , with  $\epsilon = 5$ . These  $\epsilon$  values are both in a range where asymmetry changes little with  $\epsilon$ ; hence their asymmetries can be reliably compared. We nominally confirm, then, the results of A96 that resolution degradation of asymmetry for distant galaxies observed with HST is not a significant effect *if the highest available resolutions are obtained*. We note, however, that  $\epsilon$  for distant galaxies in the HDF is just on the edge of being acceptable for asymmetry measurements. For  $q_0 < 0.5$   $\epsilon$  remains above 1, but for coarser pixel sampling  $\epsilon$  quickly falls below 1 – an issue particularly germane to NICMOS imaging data unless it is properly over-sampled.

Our computations of how the angular diameter will change as a function of redshift, illustrated in Figure 20, shows that galaxies at any redshift imaged with the *Hubble Space Telescope* can have their

asymmetries reliably computed with the suitable instrument. Even with excellent seeing on ground-based telescopes (e.g. WIYN 3.5m telescope in 0.6" seeing), asymmetry measurements can only be computed reliably out to  $z \approx 0.1$ . This shows the importance of instruments like *HST* and the *NGST* for morphological studies of high redshift galaxies. Similarly, high-order adaptive optics on large ground-based telescope will permit asymmetry measurements at large distances.

A caveat worth noting is that our simulations are based only on large, luminous galaxies. There exists the possibility that physically small galaxies have a systematically different power spectrum of luminosity fluctuations due to a scale-dependence on the number of large star-forming sites (Elmegreen & Efremov 1996). If so, our prescription based on a single  $\epsilon$  index may be overly simplistic.

## 6. Conclusions

We have describe the use of the  $180^\circ$  rotational asymmetry parameter for both physical and morphological diagnostic uses, and placed its computation on a firm basis to allow comparisons between nearby and high redshift galaxies. We tested several methods of computing rotational asymmetry, concluding that a substantially modified version of Abraham *et al.*'s (1996a) method correlated best with physical parameters such as color. The three critical modifications which we have developed here include: (1) an unambiguous and robust definition of a center of rotation; (2) a new method for correcting for noise which uses the same minimization method that is independently applied to the source; and (3) a well-defined radius within which asymmetry is measured. We artificially redshift galaxies to determine the dependence of our asymmetry measure on resolution and S/N asymmetry measurements. As expected, distance effects a galaxy's asymmetry measurement by making the galaxy more symmetric. With this revised rotational asymmetry algorithm, we estimated via simulations that asymmetry can be robustly measured down to an integrated S/N of 100 (as measured within the half-light radius), and with spatial resolution above  $0.5 h_{75}^{-1}$  kpc.

We also investigated the asymmetries computed as a function of the rotation angle,  $\phi$ , finding a strong minimum in asymmetries at a rotation angle of  $180^\circ$ , and maxima near  $90^\circ$ . To first order, these asymmetry rotation profiles are remarkably similar from galaxy to galaxy. To higher order, variations in these profiles undoubtedly offer further information for probing the light distributions of galaxies. We also find different behavior in the asymmetry of a galaxy as a function of its radius. Elliptical galaxies have a modest decline in asymmetry with increasing radius, while later type galaxies have a pronounced, and opposite trend.

We also find that  $180^\circ$  asymmetries correlate well with Hubble morphological type, color, and concentration. We suggest that the color-asymmetry relation for galaxies is a fundamental one that can be exploited in several different ways to obtain information about galaxies. From the color-asymmetry diagram alone, we are able to distinguish between spirals, ellipticals, edge-on galaxies, as well as interacting galaxies. The  $90^\circ$  asymmetries correlate strongly with ellipticity (b/a), and can be used to tighten further the correlation of color to asymmetry.

We find no correlation between the absolute magnitude or van den Bergh (1960) luminosity class and the asymmetry parameter of a galaxy. Asymmetry, which appears to be closely related to color, and hence the relative youth of a galaxy's stellar population, appears to be a morphological indicator perpendicular to this luminosity class. While the degree of asymmetry represents an indicator roughly parallel to the Hubble sequence, our expectation is that asymmetry can be used in conjunction with other quantitative

parameters to develop a new, refined morphological classification. Such a classification would have a more directly interpretable physical basis, but need not – and indeed, should not – be forced to duplicate the Hubble sequence.

We thank Greg Wirth for several stimulating conversations on computing asymmetry in a non-biased way. Both CJC and MAB thank Richard G. Kron for his ideas on galaxy morphology, the Hubble sequence, and for his encouragement over the years. We thank the referee, Roberto Abraham for his thorough reading of the manuscript, and for useful comments that improved the presentation of this paper. This research was supported by NASA LTSA grant NAG5-6043, STScI grants AR-7518 and GO-7875, and research funds from the UW graduate school (MAB); Space Telescope Science Institute (STScI) is operated by Association of Universities for Research in Astronomy, Inc., under NASA contract NAS5-26555. CJC acknowledges the hospitality of Mark Dickinson and STScI where part of this work was completed.

## REFERENCES

- Abraham, R.G., van den Bergh, S., Galzebrook, K. Ellis, R.S., Santiago, B. X., Surma, P., and Griffiths, R. E. 1996a, *ApJs*, 107, 1 (A96)
- Abraham, R. G., Tanvir, N. R., Santiago, B. X., Ellis, R.S., Glazebrook, K., and van den Bergh, S. 1996b, *MNRAS*, 279, L47
- Abraham, R. G., Valdes, F., Yee, H.K.C., van den Bergh, S., 1994, *ApJ*, 432, 75
- Baldwin, J.E., Lynden-Bell, D., & Sancisi, R. 1980, *MNRAS*, 193, 313
- Bershady, M. A. 1995, *AJ*, 109, 87
- Bershady, M. A., Hereld, M., Kron, R. G., Koo, D. C., Munn, J. A., Majewski, S. R. 1994, *AJ*, 108, 870
- Bershady, M. A., Lowenthal, J., Koo, D. C. 1998, *ApJ*, 550, 50
- Bromley, B. C., Press, W. H., Huan, L., Krishner, R. P. 1998, *ApJ*, 505, 25
- Burda, P. & Feitzinger, J.V., 1992, *A&A*, 261, 697
- Connolly, A. J., Szalay, A. S., Bershady, M. A., Kinney, A. L., Calzetti, D. 1995, *AJ*, 110, 1071
- Conselice, C. J. *PASP*, 1997, 109, 1251 (C97)
- Conselice, C. J., & Bershady, M.A., in “After the Dark Ages, when galaxies were Young:  $2 < z < 5$ ”. ed. S. Holt, University of Maryland Press, College Park, p. 225
- Curtis, H., 1918, *Publications of the Lick Observatory*, 13, 12
- Dahari, O., 1985, *ApJS*, 57, 643
- de Vaucouleurs, G. 1959, *Handbook of Physics*, 53, 311
- de Vaucouleurs, G., de Vaucouleurs, A., Corwin, H. G., Buta, R. J., Paturel, G., & Fouqué, P. 1991, *Third Reference Catalog of Bright Galaxies* (Springer, New York)
- Doi, M., Fukugita, M., Okamura, S. 1993, *MNRAS*, 264, 832
- Dressler, A., Gunn, J.E. 1992, *ApJS*, 78, 1
- Elmegreen, B.G., Efremov, Y.N., 1996, *ApJ*, 466, 802
- Elmegreen, B.G., Elmegreen, D.M. & Montenegro, L. 1992, *ApJS*, 79, 37
- Elmegreen, D.M., & Elmegreen, B.G. 1982, *MNRAS*, 201, 1021
- Ferguson, A.M.N., Wyse, R.G., Gallagher, J.S., & Hunter, D.A., 1998, *ApJ*, 506, L19.
- Folkes, S. R., Lahav, O., Maddox, S. J. 1996, *MNRAS*, 283, 651
- Frei, Z., Guhathakurta, P., Gunn, J. E., and Tyson, J. A. 1996, *AJ*, 111, 1
- Gullixson, C. A., Boeshaar, P. C., Tyson, J.A. & Seitzer, P. 1995, *ApJS*, 99, 281, 1995, *ApJS*, 99, 281
- Han, M., 1995, *ApJ*, 442, 504
- Hodge, P.W., & Kennicutt, R.C. Jr., 1983, *ApJ*, 267, 563
- Hubble, E. P., 1926, *ApJ*, 64, 321
- Hubble, E. P., 1936, *The Realm of the Nebulae*, Yale University Press
- Huchra, J. P. 1977, *ApJS*, 35, 171
- Jangren, A., Bershady, M.A., Conselice, C.J., Koo, D.C., & Guzmán, R. 1999, in preparation

- Kornreich, D.A., Haynes, M.P., & Lovelace, R.V.E., 1998, *AJ*, 116, 2154
- Koopmann, R.A., & Kenney, J.D.P, 1998, *ApJ*, 497, 75L
- Kormendy, J., Bender, R., 1996, *ApJ*, 464, 119L
- Kron, R. G. 1995, in “The Deep Universe,” Saas-Fee Advanced Course 23, (Springer), 233
- Lauer, T.R., Ajhar, E.A., Byun, Y.-I., Dressler, A., Faber, S.M., Grillmair, C., Kormendy, J., Richstone, D., & Tremaine, S., 1995, *AJ*, 110, 2622
- Morgan, W.W, 1958, *PASP*, 70, 364
- Morgan, W.W., 1959, *PASP*, 71, 394
- Naim, A., Lahav, O., Sodre L., Jr., Storrie-Lombardi, M. C. 1995, *MNRAS*, 275, 567
- Naim, A., and Lahav, O. 1997, *MNRAS*, 286, 969
- Odewahn, S. C. 1995, *PASP*, 107, 770
- Odewahn, S. C., Windhorst, R. A., Driver, S. P., and Keel, W. C., 1996, *ApJ*, 472, L13
- Okamura, S., Kodaira, K., & Watanabe, M. 1984, *ApJ*, 280, 7
- Petrosian, V., 1976, *ApJ*, 209, L1
- Rauscher, B.J., 1995, *AJ*, 109, 1608
- Richter, O.-G., & Sancisi, R., 1994, *A&A*, 290L, 9
- Rix, H.-W., & Zaritsky, D. 1995, *ApJ*, 447, 82
- Ronen, S., Aragon-Salamanca, A., Lahav, O. 1999, *MNRAS*, 303, 284
- Rudnick, G., Rix, H.-W., 1998, *AJ*, 116, 1163
- Sandage, A. R., 1961, *The Hubble Atlas of Galaxies*, Carnegie Inst. of Washington, Publ. No. 618
- Schade, D. Lilly, S. J., Crampton, D., Hammer, F., Le Fevre, O., and Tresse, L. 1995, *ApJ*, L1
- Schweizer, F. 1976a, *ApJS*, 31, 313
- Schweizer, F. 1976b, *ApJ*, 168, 333
- Serra-Ricart, M., Calbet, X., Garrido, L., and Gaitan, V. 1993, *AJ*, 106, 1685
- Spiekermann, G. 1992, *AJ*, 103, 2102
- Storrie-Lombardi, M. C., Lahav, O., Sodre, L., Jr., Storrie-Lombardi, L. J. 1992, *MNRAS*, 259, 8
- Tully, R. B. 1988, *Nearby Galaxies Catalogue* (Cambridge University Press, Cambridge)
- van den Bergh, S., Abraham, R. G., Ellis, R. S., Tanvir, N. R., Santiago, B. X., and Glazebrook, K. G., 1996, *AJ*, 112, 359
- van den Bergh, S., *ApJ*, 1960a, 131, 215
- van den Bergh, S., *ApJ*, 1960b, 131, 558
- Vorontsov-Velyaminov, B.A., 1977, *A&AS*, 28, 1
- Watanabe, M., Kodaira, K., Okamura, S., 1985, *ApJ*, 292, 72
- Whitmore, B.C., 1984, *ApJ*, 278, 61
- Wu, K. L., & Faber, S.M., Lauer, T. 1997, *BAAS*, 191, 105.10
- Zaritsky, D., Zabludoff, A. I., Willick, J. A. 1995, *AJ*, 110, 1602

TABLE 1  
ASYMMETRIES AND PHYSICAL DATA FOR FREI ET AL. LOWELL SAMPLE

Index	NGC #	Type	Notes	A(R) <sub>180</sub>	A(J) <sub>180</sub>	A(R) <sub>90</sub>	A(J) <sub>90</sub>	(B - V)	D(Mpc)	M <sub>B</sub>
1	2683	SA(rs)b	EO	0.18±0.01	0.23±0.01	1.06±0.02	1.01±0.02	0.89	5.7	-18.96
2	2715	SAB(rs)c		0.18±0.02	0.23±0.02	0.81±0.04	0.84±0.03	0.54	20.4	-20.08
3	2768	SO(1/2)	liner	0.03±0.01	0.02±0.01	0.62±0.03	0.65±0.04	0.92	23.7	-21.13
4	2775	Scd		0.05±0.01	0.07±0.01	0.15±0.02	0.17±0.03	0.87	17.0	-20.13
5	2976	SAc	pec	0.13±0.02	0.20±0.01	0.74±0.03	0.82±0.02	0.64	2.1	-16.13
6	2985	(R)SA(rs)ab		0.05±0.01	0.05±0.03	0.10±0.03	0.09±0.06	0.71	22.4	-20.65
7	3077	I0	pec	0.22±0.00	0.25±0.01	0.29±0.02	0.29±0.02	0.69	2.1	-16.13
8	3079	SB(s)c	EO, Sy2	0.48±0.01	0.53±0.01	...	...	0.68	20.4	-21.01
9	3147	SA(rs)bc	Sy2	0.09±0.01	0.09±0.04	0.09±0.05	0.03±0.13	0.79	40.9	-21.73
10	3166	SA(rs)0/a	liner	0.06±0.00	0.07±0.02	0.21±0.01	0.18±0.02	0.92	22.0	-20.22
11	3184	SAB(rs)cd		0.17±0.05	0.24±0.04	0.25±0.09	0.37±0.13	0.58	8.7	-19.34
12	3344	(R)SAB(r)bc		0.22±0.01	0.15±0.03	0.21±0.04	0.12±0.11	0.58	6.1	-18.47
13	3351	SB(r)b		0.06±0.01	0.09±0.01	0.18±0.03	0.20±0.03	0.80	8.1	-19.26
14	3368	SAB(rs)ab	Sy	0.07±0.01	0.09±0.01	0.38±0.02	0.35±0.03	0.84	8.1	-19.62
15	3377	E5-6		0.02±0.01	0.03±0.02	0.46±0.04	0.45±0.03	0.84	8.1	-18.55
16	3379	E1		0.02±0.01	0.02±0.01	0.10±0.02	0.09±0.02	0.94	8.1	-19.39
17	3486	SAB(r)c	Sy2	0.14±0.02	0.16±0.01	0.25±0.06	0.26±0.05	0.51	7.4	-18.61
18	3556	SB(s)cd	EO	0.25±0.01	0.26±0.02	...	...	0.66	14.1	-20.77
19	3596	SAB(rs)c		0.15±0.01	0.18±0.02	0.22±0.02	0.23±0.03	...	23.0	-20.31
20	3623	SAB(rs)a	liner	0.13±0.01	0.15±0.01	0.88±0.03	0.87±0.04	0.92	7.3	-19.81
21	3631	SA(s)c		0.16±0.02	0.23±0.01	0.20±0.04	0.28±0.03	0.58	21.6	-20.69
22	3672	SA(s)c		0.23±0.01	0.27±0.02	0.86±0.03	0.83±0.04	0.68	28.4	-21.17
23	3675	SA(s)b		0.13±0.03	0.25±0.03	0.50±0.08	0.54±0.15	...	12.8	-19.84
24	3726	SAB(r)c		0.18±0.03	0.23±0.04	0.44±0.08	0.48±0.04	0.48	17.0	-20.35
25	3810	SA(rs)c		0.19±0.01	0.22±0.01	0.36±0.02	0.38±0.03	0.54	16.9	-20.11
26	3877	SA(s)c	EO	0.22±0.01	0.24±0.01	1.22±0.03	1.19±0.04	0.80	17.0	-20.25
27	3893	SAB(rs)c		0.19±0.01	0.25±0.01	0.32±0.02	0.37±0.02	...	17.0	-20.27
28	3938	SA(s)c		0.19±0.01	0.20±0.01	0.18±0.02	0.21±0.03	0.51	17.0	-20.26
29	3953	SB(r)bc	liner, HII	0.13±0.01	0.16±0.01	0.56±0.04	0.60±0.04	0.76	17.0	-20.63
30	4013	Sb	EO	0.06±0.12	0.03±0.10	0.05±0.15	-0.02±0.15	0.96	17.0	-19.55
31	4030	SA(s)bc		0.11±0.01	0.15±0.01	0.21±0.02	0.25±0.02	...	25.9	-20.27
32	4088	SAB(rs)bc		0.41±0.01	0.43±0.01	0.97±0.02	0.96±0.03	0.58	17.0	-20.47
33	4123	SB(r)c		0.14±0.03	0.18±0.02	0.49±0.08	0.51±0.08	0.59	25.3	-20.25
34	4125	E6	pec, liner	0.03±0.02	0.04±0.01	0.30±0.09	0.36±0.08	0.91	24.2	-21.35
35	4136	SAB(r)c		0.14±0.02	0.18±0.02	0.13±0.05	0.15±0.06	...	9.7	-18.23
36	4144	SAB(s)cd?	EO	0.14±0.03	0.17±0.02	0.95±0.08	0.97±0.09	0.43	4.1	-16.87
37	4157	SAB(s)b?	EO	0.29±0.01	0.27±0.04	1.24±0.04	0.81±0.13	0.80	17.0	-20.15
38	4242	SAB(s)dm		0.21±0.06	0.15±0.07	0.35±0.10	0.43±0.21	0.54	7.5	-17.91
39	4340	SB(r)0+		0.02±0.01	0.01±0.01	0.23±0.04	0.23±0.04	0.91	16.8	-19.17
40	4365	E3		0.03±0.01	0.00±0.02	0.22±0.03	0.10±0.10	0.95	16.8	-20.52
41	4374	E1		0.01±0.01	0.01±0.01	...	...	0.94	16.8	-20.95
42	4406	S0(3)/E3		0.03±0.02	0.02±0.02	...	...	0.93	16.8	-21.15
43	4429	SA(r)0+		0.05±0.01	0.05±0.02	0.66±0.02	0.57±0.06	0.96	16.8	-20.08
44	4442	SB(s)0		0.02±0.00	0.05±0.02	0.43±0.01	0.42±0.02	0.93	16.8	-19.84
45	4449	IBm		0.26±0.01	0.29±0.01	0.70±0.03	0.74±0.03	0.41	3.0	-17.66
46	4450	SA(s)ab	liner	0.04±0.01	0.06±0.01	0.41±0.04	0.36±0.06	0.80	16.8	-20.36
47	4472	E2/S0(2)		0.02±0.01	0.01±0.00	0.14±0.02	0.14±0.02	0.96	16.8	-21.82
48	4477	SB(s)0		0.02±0.01	0.01±0.01	0.17±0.02	0.16±0.03	0.94	16.8	-19.87
49	4486	E2	pec	0.01±0.01	0.02±0.01	0.07±0.02	0.07±0.03	0.93	16.8	-21.64
50	4487	SAB(rs)cd		0.12±0.03	0.13±0.05	0.32±0.07	0.27±0.10	...	19.9	-20.19
51	4526	SAB(s)0		0.06±0.00	0.07±0.01	0.62±0.01	0.59±0.02	0.95	16.8	-20.55
52	4564	E6		0.02±0.01	0.02±0.03	0.63±0.03	0.55±0.05	0.90	16.8	-19.30
53	4593	(R)SB(rs)b	Sy1	0.09±0.01	0.09±0.01	0.47±0.04	0.45±0.04	...	39.5	-21.58
54	4594	SA(s)a	liner EO	0.16±0.01	0.18±0.03	0.60±0.03	0.51±0.09	0.98	20.0	-22.98
55	4621	E5		0.02±0.01	0.01±0.01	0.33±0.02	0.33±0.02	0.92	16.8	-20.45
56	4636	E/S0-1	liner	0.02±0.01	0.01±0.01	0.13±0.04	0.11±0.05	0.92	17.0	-20.68
57	4710	SA(r)0+	EO	0.05±0.01	0.05±0.01	1.11±0.01	1.11±0.02	0.88	16.8	-19.36
58	4731	SB(s)cd		0.18±0.04	0.27±0.04	0.95±0.12	0.96±0.04	0.41	25.9	-21.17
59	4754	SB(r)0-		0.01±0.00	0.00±0.02	0.20±0.01	0.17±0.02	0.90	16.8	-19.74
60	4826	(R)SA(rs)ab	Sy2	0.15±0.01	0.20±0.01	0.48±0.04	0.53±0.02	0.84	4.1	-19.15
61	4861	SB(s)m		0.12±0.11	0.14±0.07	0.22±0.12	0.16±0.11	0.58	17.8	-18.87
62	4866	SA(r)0+	EO, liner	0.04±0.02	0.04±0.03	0.84±0.04	0.88±0.04	0.90	16.0	-19.06
63	5005	SAB(rs)bc	Sy2	0.14±0.01	0.20±0.01	0.78±0.03	0.80±0.02	0.80	21.3	-21.27
64	5204	SA(s)m		0.20±0.03	0.25±0.06	0.37±0.06	0.38±0.13	0.41	4.8	-16.79
65	5248	SAB(rs)bc	HII	0.18±0.01	0.20±0.02	0.56±0.03	0.54±0.07	0.65	22.7	-21.07
66	5322	E3-4	liner	0.02±0.02	0.02±0.01	0.29±0.06	0.33±0.06	0.89	31.6	-21.66
67	5334	SB(rs)c		0.08±0.12	0.09±0.12	-0.07±0.14	-0.09±0.14	...	24.7	-19.66
68	5364	SA(rs)bc	pec, HII	0.15±0.03	0.15±0.02	0.36±0.07	0.31±0.09	0.61	25.5	-21.17
69	5371	SA(rs)bc	liner	0.14±0.01	0.14±0.02	0.42±0.03	0.38±0.05	0.68	37.8	-21.57
70	5377	(R)SB(s)a		0.03±0.01	0.07±0.02	0.67±0.03	0.59±0.06	0.89	31.0	-20.69
71	5585	SAB(s)d		0.23±0.02	0.16±0.03	0.44±0.06	0.34±0.09	0.46	7.0	-17.96
72	5669	SAB(rs)cd		0.18±0.03	0.19±0.06	0.42±0.05	0.38±0.09	...	24.9	-19.88
73	5701	(R)SB(rs)0/a		0.04±0.00	0.05±0.02	0.27±0.01	0.27±0.02	0.84	26.1	-20.35
74	5746	SAB(rs)b	EO	0.26±0.01	0.25±0.01	...	...	0.97	29.4	-21.73
75	5792	SB(rs)b		0.31±0.02	0.36±0.03	0.65±0.04	0.72±0.07	0.78	30.6	-20.83
76	5813	E1-2		0.02±0.01	0.03±0.02	0.20±0.03	0.18±0.05	0.94	28.5	-20.77
77	5850	SB(r)b		0.07±0.01	0.08±0.03	0.29±0.06	0.28±0.11	0.74	28.5	-20.69
78	5985	SAB(r)b	liner	0.14±0.01	0.11±0.02	0.67±0.03	0.49±0.05	0.74	39.2	-21.42
79	6015	SA(s)cd	HII	0.15±0.01	0.19±0.02	0.65±0.03	0.63±0.05	0.56	17.5	-20.05
80	6118	SA(s)cd		0.13±0.02	0.14±0.04	0.80±0.06	0.67±0.10	0.64	25.4	-20.62
81	6384	SAB(r)bc		0.14±0.01	0.13±0.02	0.40±0.04	0.34±0.07	0.61	26.6	-21.31
82	6503	SA(s)cd	liner, HII	0.15±0.01	0.23±0.01	1.04±0.01	1.08±0.03	0.68	6.1	-18.64

TABLE 2  
ASYMMETRIES AND PHYSICAL DATA FOR FREI ET AL. PALOMAR SAMPLE

Index	NGC #	Type	Notes	A(g) <sub>180</sub>	A(r) <sub>180</sub>	A(i) <sub>180</sub>	A(r) <sub>90</sub>	(B-V)	D(Mpc)	M <sub>B</sub>
1	2403	SAB(s)cd		0.30±0.02	0.17±0.03	0.10±0.05	0.53±0.00	0.47	4.2	-19.68
2	2541	SA(s)cd		0.16±0.10	0.17±0.10	0.08±0.13	0.56±0.02	0.46	10.6	-18.37
3	2903	SAB(rs)bc	HII	0.22±0.01	0.16±0.01	0.12±0.02	0.63±0.00	0.67	6.3	-19.85
4	3031	SA(s)ab	LINER	0.08±0.01	0.06±0.01	0.05±0.01	0.63±0.00	0.95	1.4	-18.29
5	3198	SB(rs)c		0.14±0.05	0.12±0.04	0.07±0.06	0.75±0.00	0.54	10.8	-19.62
6	3319	SB(rs)cd?	HII	0.13±0.09	0.10±0.09	0.04±0.13	0.83±0.01	0.41	11.5	-18.71
7	4178	SA(rs)dm		0.24±0.05	0.21±0.04	0.13±0.07	1.00±0.00	0.49	16.8	-19.77
8	4189	SAB(rs)cd?	EO	0.33±0.03	0.32±0.03	0.22±0.04	0.44±0.00	0.77	16.8	-18.72
9	4192	SAB(s)ab	HII	0.25±0.03	0.20±0.02	0.14±0.03	0.44±0.00	0.81	16.8	-21.08
10	4216	SAB(s)b	HII,EO	0.28±0.01	0.21±0.01	0.15±0.01	0.64±0.00	0.98	16.8	-20.96
11	4254	SA(s)c		0.36±0.01	0.31±0.01	0.22±0.02	0.36±0.00	0.57	16.8	-20.84
12	4258	SAB(s)bc	syft	0.23±0.01	0.19±0.01	0.13±0.01	0.58±0.00	0.69	6.8	-20.59
13	4303	SAB(rs)bc	HII	0.30±0.01	0.28±0.01	0.20±0.02	0.40±0.00	0.53	15.2	-20.71
14	4321	SAB(s)bc	HII	0.18±0.03	0.16±0.02	0.10±0.04	0.35±0.00	0.70	16.8	-21.13
15	4394	(R)SB(r)b	LINER	0.06±0.01	0.05±0.01	0.04±0.01	0.23±0.00	0.85	16.8	-19.49
16	4414	SA(rs)c?		0.21±0.01	0.15±0.01	0.10±0.01	0.43±0.00	0.84	9.7	-19.12
17	4498	SAB(s)d		0.16±0.04	0.15±0.04	0.10±0.06	0.75±0.00	...	16.8	-18.93
18	4501	SA(rs)b	syft	0.21±0.02	0.16±0.01	0.12±0.02	0.52±0.00	0.73	16.8	-21.23
19	4527	SAB(s)bc	HII	0.25±0.03	0.20±0.02	0.17±0.03	0.63±0.00	0.86	13.5	-19.72
20	4535	SAB(s)c		0.15±0.04	0.13±0.03	0.08±0.06	0.39±0.00	0.63	16.8	-20.60
21	4548	SB(rs)b	LINER	0.08±0.03	0.06±0.03	0.05±0.04	0.25±0.00	0.81	16.8	-20.28
22	4559	SAB(rs)cd		0.22±0.03	0.20±0.02	0.11±0.04	0.69±0.00	0.45	9.7	-20.07
23	4569	SAB(rs)ab	LINER	0.15±0.03	0.13±0.02	0.09±0.03	0.69±0.00	0.72	16.8	-21.27
24	4571	SA(r)d		0.08±0.07	0.07±0.06	0.03±0.09	0.20±0.01	0.51	16.8	-19.38
25	4579	SAB(rs)b	LINER	0.06±0.02	0.05±0.01	0.04±0.02	0.27±0.00	0.82	16.8	-20.67
26	4651	SA(rs)c	LINER	0.11±0.03	0.10±0.02	0.07±0.03	0.33±0.00	0.57	16.8	-20.07
27	4654	SAB(rs)cd		0.20±0.04	0.19±0.04	0.11±0.06	0.63±0.00	0.60	16.8	-20.31
28	4689	SA(rs)bc		0.07±0.08	0.05±0.06	0.02±0.08	0.23±0.01	0.65	16.8	-19.62
29	4725	SAB(r)ab	pec	0.08±0.05	0.07±0.03	0.05±0.04	0.34±0.00	0.72	12.4	-20.65
30	5033	SA(s)c	syft	0.18±0.05	0.15±0.03	0.10±0.04	0.53±0.00	0.55	18.7	-21.03
31	5055	SA(rs)bc	HII	0.19±0.02	0.14±0.02	0.10±0.02	0.43±0.00	0.72	7.2	-20.14

TABLE 3  
ASYMMETRIES CALCULATED AT VARIOUS RADII FOR THE FREI ET AL. LOWELL SAMPLE<sup>a</sup>

Index	NGC #	$A[\eta = 0.8]$	$A[\eta = 0.5]$	$A[\eta = 0.2]$	$A[g = 20\%]$	$A[g = 50\%]$	$A[g = 80\%]$	$A_\eta$ <sup>b</sup>	$A_g$ <sup>c</sup>
1	NGC 2683	0.120	0.155	0.183	0.144	0.161	0.183	0.172	0.175
2	NGC 2715	0.486	0.146	0.175	0.098	0.137	0.149	0.206	0.192
3	NGC 2768	0.021	0.015	0.026	0.015	0.014	0.025	0.036	0.029
4	NGC 2775	0.031	0.019	0.052	0.018	0.051	0.051	0.062	0.057
5	NGC 2976	0.119	0.135	0.127	0.116	0.127	0.134	0.119	0.119
6	NGC 2985	0.031	0.039	0.046	0.039	0.045	0.045	0.046	0.046
7	NGC 3077	0.044	0.138	0.219	0.139	0.209	0.213	0.222	0.218
8	NGC 3079	0.108	0.324	0.476	0.231	0.394	0.472	0.483	0.478
9	NGC 3147	0.036	0.038	0.090	0.051	0.079	0.090	0.098	0.094
10	NGC 3166	0.033	0.040	0.056	0.040	0.060	0.055	0.049	0.052
11	NGC 3184	0.043	0.151	0.165	0.089	0.146	0.160	0.165	0.165
12	NGC 3344	0.045	0.032	0.218	0.196	0.176	0.207	0.219	0.219
13	NGC 3351	0.137	0.102	0.059	0.094	0.056	0.057	0.061	0.059
14	NGC 3368	0.057	0.070	0.070	0.076	0.059	0.068	0.069	0.069
15	NGC 3377	0.044	0.038	0.021	0.034	0.023	0.021	0.027	0.024
16	NGC 3379	0.028	0.020	0.020	0.020	0.016	0.019	0.028	0.024
17	NGC 3486	0.047	0.084	0.139	0.051	0.099	0.130	0.138	0.139
18	NGC 3556	0.107	0.252	0.250	0.246	0.250	0.250	0.250	0.250
19	NGC 3596	0.035	0.152	0.154	0.106	0.126	0.158	0.148	0.146
20	NGC 3623	0.044	0.107	0.127	0.077	0.123	0.124	0.123	0.126
21	NGC 3631	0.030	0.052	0.162	0.064	0.120	0.168	0.147	0.145
22	NGC 3672	0.089	0.196	0.227	0.109	0.196	0.222	0.219	0.224
23	NGC 3675	0.071	0.238	0.133	0.231	0.140	0.133	0.133	0.133
24	NGC 3726	0.027	0.036	0.176	0.088	0.134	0.161	0.185	0.183
25	NGC 3810	0.043	0.107	0.194	0.077	0.155	0.181	0.192	0.194
26	NGC 3877	0.097	0.190	0.224	0.219	0.178	0.200	0.224	0.221
27	NGC 3893	0.027	0.100	0.194	0.075	0.105	0.193	0.183	0.186
28	NGC 3938	0.011	0.127	0.189	0.043	0.098	0.165	0.195	0.195
29	NGC 3953	0.030	0.035	0.127	0.049	0.078	0.114	0.122	0.124
30	NGC 4013	0.079	0.101	0.064	0.055	0.064	0.064	0.064	0.064
31	NGC 4030	0.028	0.097	0.108	0.067	0.097	0.107	0.103	0.105
32	NGC 4088	0.111	0.285	0.408	0.218	0.252	0.369	0.386	0.391
33	NGC 4123	0.080	0.066	0.135	0.061	0.109	0.134	0.140	0.140
34	NGC 4125	0.018	0.017	0.026	0.017	0.015	0.018	0.051	0.026
35	NGC 4136	0.029	0.121	0.140	0.049	0.115	0.137	0.136	0.137
36	NGC 4144	0.034	0.096	0.138	0.058	0.092	0.126	0.154	0.147
37	NGC 4157	0.122	0.260	0.287	0.247	0.273	0.283	0.312	0.304
38	NGC 4242	0.043	0.100	0.209	0.070	0.104	0.209	0.209	0.209
39	NGC 4340	0.029	0.030	0.022	0.029	0.019	0.021	0.027	0.025
40	NGC 4365	0.022	0.015	0.025	0.015	0.020	0.022	0.033	0.026
41	NGC 4374	0.021	0.020	0.011	0.016	0.012	0.012	0.014	0.013
42	NGC 4406	0.021	0.018	0.031	0.015	0.021	0.029	0.031	0.031
43	NGC 4429	0.061	0.094	0.053	0.094	0.068	0.052	0.057	0.055
44	NGC 4442	0.023	0.022	0.016	0.022	0.018	0.017	0.019	0.018
45	NGC 4449	0.085	0.219	0.263	0.149	0.225	0.264	0.258	0.261
46	NGC 4450	0.027	0.037	0.040	0.037	0.039	0.040	0.053	0.050
47	NGC 4472	0.015	0.010	0.017	0.010	0.010	0.014	0.026	0.019
48	NGC 4477	0.030	0.024	0.021	0.024	0.016	0.020	0.028	0.022
49	NGC 4486	0.010	0.018	0.009	0.019	0.011	0.010	0.011	0.009
50	NGC 4487	0.048	0.094	0.123	0.062	0.079	0.113	0.113	0.113
51	NGC 4526	0.070	0.092	0.058	0.092	0.078	0.059	0.053	0.056
52	NGC 4564	0.036	0.032	0.016	0.034	0.022	0.016	0.014	0.014
53	NGC 4593	0.054	0.046	0.085	0.037	0.034	0.071	0.089	0.088
54	NGC 4594	0.032	0.065	0.164	0.085	0.205	0.179	0.159	0.163
55	NGC 4621	0.039	0.034	0.020	0.032	0.019	0.020	0.020	0.019
56	NGC 4636	0.016	0.013	0.019	0.012	0.012	0.015	0.021	0.020
57	NGC 4710	0.083	0.055	0.048	0.065	0.052	0.048	0.048	0.048
58	NGC 4731	0.098	0.137	0.183	0.129	0.149	0.191	0.176	0.180
59	NGC 4754	0.027	0.023	0.014	0.025	0.017	0.014	0.013	0.014
60	NGC 4826	0.077	0.297	0.148	0.369	0.210	0.161	0.139	0.144
61	NGC 4861	0.105	0.092	0.118	0.096	0.121	0.142	0.118	0.118
62	NGC 4866	0.022	0.024	0.039	0.023	0.028	0.034	0.043	0.039
63	NGC 5005	0.122	0.168	0.136	0.173	0.171	0.143	0.127	0.133
64	NGC 5204	0.117	0.153	0.197	0.111	0.156	0.166	0.370	0.318
65	NGC 5248	0.060	0.065	0.176	0.103	0.140	0.179	0.176	0.177
66	NGC 5322	0.043	0.028	0.017	0.025	0.020	0.017	0.020	0.017
67	NGC 5334	0.010	0.064	0.084	0.055	0.066	0.081	0.084	0.084
68	NGC 5364	0.011	0.121	0.152	0.077	0.116	0.138	0.147	0.147
69	NGC 5371	0.046	0.035	0.143	0.056	0.112	0.137	0.156	0.152
70	NGC 5377	0.055	0.056	0.034	0.047	0.029	0.032	0.040	0.034
71	NGC 5585	0.029	0.129	0.232	0.069	0.115	0.162	0.373	0.294
72	NGC 5669	0.019	0.165	0.182	0.052	0.093	0.162	0.193	0.196
73	NGC 5701	0.038	0.024	0.036	0.026	0.016	0.037	0.042	0.041
74	NGC 5746	0.093	0.312	0.259	0.294	0.311	0.258	0.270	0.258
75	NGC 5792	0.039	0.220	0.314	0.185	0.250	0.316	0.279	0.281
76	NGC 5813	0.034	0.026	0.023	0.022	0.017	0.021	0.030	0.026
77	NGC 5850	0.022	0.028	0.068	0.028	0.029	0.052	0.083	0.074
78	NGC 5985	0.018	0.097	0.137	0.054	0.086	0.117	0.197	0.181
79	NGC 6015	0.043	0.114	0.151	0.056	0.108	0.133	0.148	0.149
80	NGC 6118	0.009	0.099	0.129	0.058	0.096	0.131	0.118	0.121
81	NGC 6384	0.031	0.027	0.136	0.037	0.081	0.113	0.147	0.141
82	NGC 6503	0.142	0.156	0.153	0.141	0.157	0.152	0.175	0.168

<sup>a</sup>All asymmetries are computed in the R band.

<sup>b</sup> $A_\eta$  is defined as  $1.5 * r[\eta(0.2)]$

<sup>c</sup> $A_g$  is defined as  $3.0 * r[g(0.5)]$ , where  $r[g(0.5)]$  is the half-light radius.



TABLE 4  
ASYMMETRIES CALCULATED AT VARIOUS RADII FOR THE FREI ET AL. PALOMAR SAMPLE<sup>a</sup>

Index	NGC #	$A[\eta(0.8)]$	$A[\eta(0.5)]$	$A[\eta(0.2)]$	$A[g(20)]$	$A[g(50)]$	$A[g(80)]$	$A_\eta$ <sup>b</sup>	$A_g$ <sup>c</sup>
1	NGC 2403	0.122	0.169	0.173	0.120	0.164	0.180	0.157	0.166
2	NGC 2541	0.026	0.150	0.171	0.059	0.145	0.176	0.157	0.160
3	NGC 2903	0.097	0.171	0.159	0.158	0.161	0.161	0.145	0.146
4	NGC 3031	0.003	0.023	0.057	0.026	0.053	0.055	0.064	0.059
5	NGC 3198	0.076	0.118	0.122	0.104	0.122	0.122	0.110	0.114
6	NGC 3319	0.073	0.102	0.100	0.111	0.080	0.104	0.073	0.081
7	NGC 4178	0.059	0.143	0.212	0.110	0.133	0.192	0.181	0.203
8	NGC 4189	0.051	0.226	0.317	0.075	0.158	0.296	0.287	0.287
9	NGC 4192	0.083	0.155	0.202	0.150	0.191	0.207	0.180	0.192
10	NGC 4216	0.009	0.078	0.209	0.139	0.250	0.218	0.187	0.213
11	NGC 4254	0.040	0.184	0.309	0.121	0.189	0.258	0.316	0.326
12	NGC 4258	0.055	0.189	0.187	0.208	0.182	0.191	0.178	0.183
13	NGC 4303	0.030	0.037	0.281	0.046	0.201	0.280	0.259	0.266
14	NGC 4321	0.057	0.114	0.159	0.080	0.139	0.160	0.151	0.151
15	NGC 4394	0.047	0.031	0.045	0.024	0.025	0.041	0.043	0.043
16	NGC 4414	0.028	0.149	0.147	0.142	0.159	0.150	0.141	0.143
17	NGC 4498	0.019	0.156	0.148	0.106	0.156	0.151	0.138	0.141
18	NGC 4501	0.018	0.153	0.163	0.158	0.155	0.163	0.152	0.154
19	NGC 4527	0.390	0.325	0.196	0.307	0.220	0.182	0.155	0.161
20	NGC 4535	0.065	0.060	0.126	0.068	0.100	0.122	0.112	0.117
21	NGC 4548	0.034	0.027	0.063	0.023	0.043	0.063	0.057	0.057
22	NGC 4559	0.081	0.146	0.196	0.126	0.139	0.172	0.187	0.194
23	NGC 4569	0.031	0.084	0.126	0.137	0.143	0.132	0.114	0.116
24	NGC 4571	0.014	0.049	0.072	0.028	0.048	0.061	0.076	0.076
25	NGC 4579	0.023	0.033	0.047	0.030	0.052	0.048	0.043	0.044
26	NGC 4651	0.035	0.099	0.104	0.078	0.105	0.099	0.094	0.095
27	NGC 4654	0.032	0.151	0.186	0.093	0.139	0.183	0.173	0.172
28	NGC 4689	0.024	0.061	0.054	0.069	0.061	0.053	0.053	0.054
29	NGC 4725	0.011	0.021	0.074	0.027	0.035	0.077	0.065	0.066
30	NGC 5033	0.046	0.097	0.145	0.142	0.133	0.141	0.131	0.134
31	NGC 5055	0.099	0.160	0.142	0.140	0.161	0.146	0.131	0.136

<sup>a</sup>All asymmetries are computed in the r band.

<sup>b</sup> $A_\eta$  is defined as  $1.5 * r[\eta(0.2)]$

<sup>c</sup> $A_g$  is defined as  $3.0 * r[g(0.5)]$ , where  $r[g(0.5)]$  is the half-light radius.

Fig. 1.— Scatter plot of the red  $180^\circ$  asymmetries computed by the RMS method (Conselice 1997) and the ABS method (Abraham *et al.* 1996a). The two methods produce similar asymmetry values, with a noticeable trend towards higher asymmetries for more asymmetric galaxies. The open symbols are Palomar sample galaxies (Gunn  $r$  band, Table 2); filled symbols are the Lowell sample galaxies ( $R$  band, Table 1).

Fig. 2.— Comparison between the  $180^\circ$  RMS asymmetry parameter computed in the  $R$  and  $B$  bands (filled symbols) and  $g$  and  $r$  bands (open symbols). The bluer band asymmetries tends to always be more asymmetric than the redder band asymmetries, and this difference increases at higher asymmetries. This indicates that young blue stars (and hence recent star formation) produce asymmetries. There is no differences in trend or scatter between the  $B$  versus  $R$  and  $g$  versus  $r$  data.

Fig. 3.— As Figure 2, but with the asymmetries computed with the ABS method. The relationship between the asymmetries does not show the prominent rise in blue asymmetries as the RMS asymmetry values.

Fig. 4.— Six representative ‘Early’-type galaxies from the *et al.* (1996) sample. From left to right: (1) the  $B_J$  or  $g$  band image. The NGC number, Hubble type,  $A_{180}(R)$ , and  $B - V$  color are listed in clockwise order starting at the bottom left corner of each image. (2) Asymmetry,  $A_{180}(R)$ , as a function of center position,  $A(x,y)$ . The grey-scale stretch is from 0.02 (white) to 0.44 (black) in every panel. The maximum asymmetry value is printed in the upper-right corner of each panel. (3)  $A_{180}(R) / A_{\max}$ , the asymmetry as a function of radius (more precisely, the square extraction box half-width) normalized by the half-light radius, for rotation angle  $\phi = 180$ , normalized by the maximum value labeled in each panel. The radius where  $\eta = 0.2$  is marked with a dotted vertical line. (4)  $A_\phi(R) / A_{\max}$ , the asymmetry as a function of rotation angle ( $-180 < \phi < 180$ ) within a radius corresponding to  $\eta = 0.2$  (see text), normalized by the maximum value.  $A_\phi(R)$  is folded every 90 degrees to show the expected inherent symmetry in an axisymmetric system. Solid lines are for  $0 < \phi < 180$  and dashed lines are for  $-180 < \phi < 0$ . The value of  $A_{90}(R)$  is labeled.

Fig. 5.— The same as Figure 4, except for 6 representative ‘Intermediate’-type galaxies.

Fig. 6.— The same as Figure 4, except for 6 representative ‘Late’-type galaxies.

Fig. 7.— The same as Figure 4, except for an irregular, disturbed and edge-on galaxy.

Fig. 8.— A representation of how asymmetry increases at lower values of S/N without noise corrections. Represented here are 35 galaxies from our sample which includes all inclinations and Hubble types from the entire sample. The vertical axis  $\Delta A(R)$  is the difference between the computed asymmetry at a given S/N (x-axis) and the original asymmetry value. The S/N is computed within the  $\eta = 0.2$  radius. The dashed lines at  $\Delta A(R) = \pm 0.1$  and the vertical line at S/N of 100 are for reference. This figure shows that without correcting for the S/N, the asymmetry of a galaxy becomes large even at moderately large S/N values.

Fig. 9.— Plot of the asymmetry within the  $\eta = 0.2$  radii as a function of the S/N as in Figure 8, except here noise corrected. Reliable values, i.e. within 0.05 of the original value, of the asymmetry can be computed with the algorithm presented in this paper down to a S/N of about 100. Dashed lines at  $\Delta A(R) = \pm 0.1$  and the vertical line at S/N of 100 are for reference.

Fig. 10.— Color-Asymmetry diagram. This physical-morphological diagram (as defined in text) can be used to determine the population of galaxies in a large sample. Labeled galaxies are undergoing interactions or galaxy mergers. Three features stand out in this diagram: (1) The early-type disks/spheriods are well separated from the late type disks. (2) The interacting galaxies deviate from the color-asymmetry sequence such that they are too asymmetric for their color. Their asymmetries are not caused solely by star formation,

but in part result from tides distorting their structure. (3) The edge-on galaxies also deviate, and generally are too asymmetric or red, both effects caused by dust lanes affecting the morphology (higher asymmetry) and the color (redder).

Fig. 11.— The relationship between  $A_{90}$  and  $A_{180}$ . Plotted here as different symbols are spheroids, early type disks, late type disks, irregulars, and edge-on galaxies. For a given range of  $A_{180}$  there is a high scatter in the  $A_{90}$  values. The edge-on galaxies stand out in this diagram as being the systems with the highest  $A_{90}$  values for their  $A_{180}$  values. There is also a fairly sharp division between spheroids/early-type disks and late-type disks. We also find no spheroids and few early type disks with  $A_{90} > 0.7$ . This type of plot can therefore be used to determine general properties of a sample of galaxies.

Fig. 12.— Plot of the asymmetries in the  $R$  and  $B$  bands computed by rotating the galaxy by  $90^\circ$  instead of the nominal  $180^\circ$ . The mean difference  $A(B)_{90} - A(R)_{90}$  is near zero for all  $A(R)_{90}$ , in contrast to  $A(B)_{180} - A(R)_{180}$ , which systematically deviates to positive values for larger  $A(R)_{180}$ . Since most galaxies are not perfectly round,  $A_{90}$  measures the ellipticity, or deviations in shape from a perfect circle. The edge-on galaxies always have the highest values of  $A_{90}$ . The consistency between the two different wavelengths indicates that contributions to  $A_{90}$  are mostly due to global shape. However, higher values are  $A(B)$ , compared with  $A(R)$ , are seen but only at the largest values of  $A_{180}$ , indicating that star formation is not a significant addition to  $A_{90}$ , but does contribute somewhat as would be expected.

Fig. 13.— Plot of the axis ratio for our sample ( $\log(b/a)$  from RC3) versus the asymmetry computed with a rotation angle of  $90^\circ$ . This strong correlation is evidence that  $A_{90}$  is primarily a measure of the azimuthal *shape* of a galaxy, rather than physical effects, such as star formation, or dynamical effects which primary cause  $A_{180}$  asymmetries. The bottom plot shows  $A_{90} - A_{180}$  plotted instead of  $A_{90}$  showing a better correlation, indicating that there is some flocculent asymmetry contributing to  $A_{90}$ . Linear regressions are for illustrative purposes.

Fig. 14.— The color-asymmetry diagram showing the distribution of galaxies with high axis ratios  $[b/a]$ . A principle cause of the scatter in the normal galaxy-sequence of Figure 10 are reddening and morphological changes that occur for inclined galaxies. The galaxies with the highest inclinations are the ones that deviate the most from this sequence.

Fig. 15.— The color corrected color-asymmetry diagram. This version of the color-asymmetry diagram uses dereddened  $(B - V)$  colors, corrected for inclination effects (de Vaucouleurs et al. 1991). The normal galaxy sequence is tighter, and many of the edge-on galaxies nearly coincide with other galaxies having similar colors and asymmetries. This figure, and Figure 14 shows how this diagram is being affected by inclination.

Fig. 16.— Asymmetry-concentration diagram. This diagram is similar to the one used by Abraham *et al.* (1996b) for galaxies in the Hubble Deep Field. The spheroids stand out in this diagram as being the symmetric and most concentrated objects, while the late disks are less concentrated and more asymmetric. There is not however, as clean a division between early and late disks as seen in the color-asymmetry diagram (Figure 12). Interestingly, nearly all of the edge-on disks fit between the two dashed lines. The four interacting galaxies still stand out in this diagram.

Fig. 17.— The asymmetry distribution as a function of Hubble T-type. There is a general increase in average asymmetry at later types, but there is a large scatter in asymmetry at each Hubble type, similar to the pattern found for most physical parameters.

Fig. 18.— (a) Top panel.  $B - V$  vs  $B$  absolute magnitude, with different symbols distinguishing morphological

types as in Figure 16. (B) Bottom panel. The red asymmetry parameter ( $R$  or  $r$ ) plotted as a function of the absolute magnitude. As shown in Conselice (1997) there is little correlation between the intrinsic brightness and asymmetry of a galaxy for the narrow range of magnitudes in the Frei *et al.* sample.

Fig. 19.— Asymmetry as a function of spatial resolution. The parameter  $\epsilon$  is the ratio of the angular diameter corresponding to  $0.5 h_{75}^{-1}$  kpc divided by the angular resolution. From this plot it can be seen that the asymmetry of a galaxy is measurable to better than 10% down to  $\epsilon \approx 1$ .

Fig. 20.— Apparent size versus redshift for a metric length of  $0.5 h_{75}^{-1}$  kpc and several values of  $\Omega$  composed of non-relativistic matter and a cosmological constant. The solid lines are for  $\Omega_{total} = 0.1$  and  $0.3$ , and  $\Omega_{\Lambda} = 0$ , i.e.  $q_0 = 0.05$  and  $0.15$  for the bottom and top solid curves, respectively. The dashed curves are for  $\Omega_{total} = 1$ , with  $\Omega_{\Lambda} = 0.9$  and  $0.3$ , i.e.  $q_0 = -0.850$  and  $-0.550$  for the bottom and top dashed curves, respectively. Accessible apparent sizes for different instruments classes are indicated by the shading: modern ground-based telescopes at good sites in ambient conditions (ground/ambient, e.g. WIYN); ground-based telescopes with adaptive optics (ground/AO, e.g. CFHT); space-based telescopes (HST, NGST). Since scales of  $0.5 h_{75}^{-1}$  Mpc must be resolved to accurately measure rotational asymmetries, cosmological measurements of asymmetry require spatial resolutions of 0.1 arcsec or better.

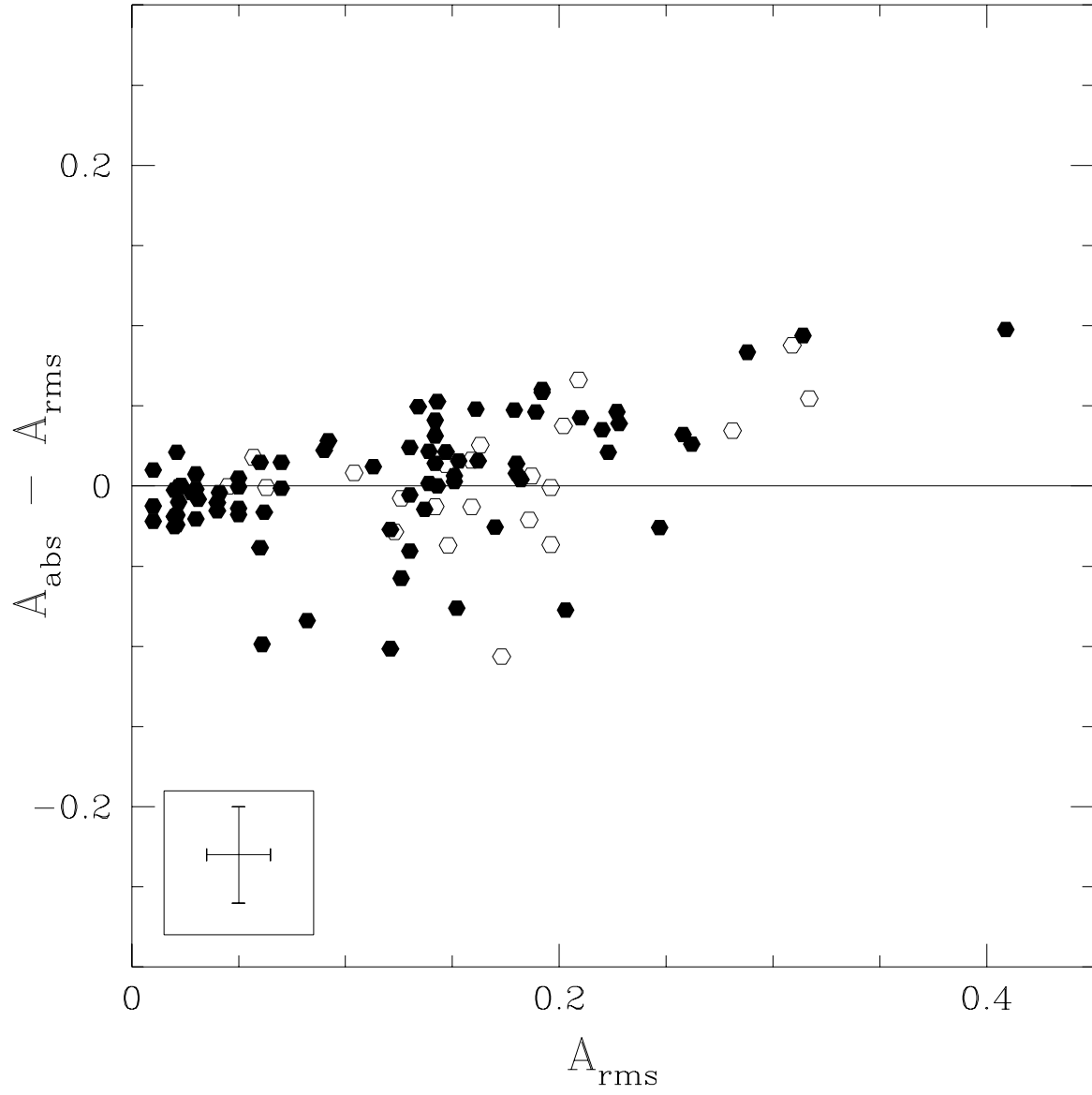


Fig. 1.—

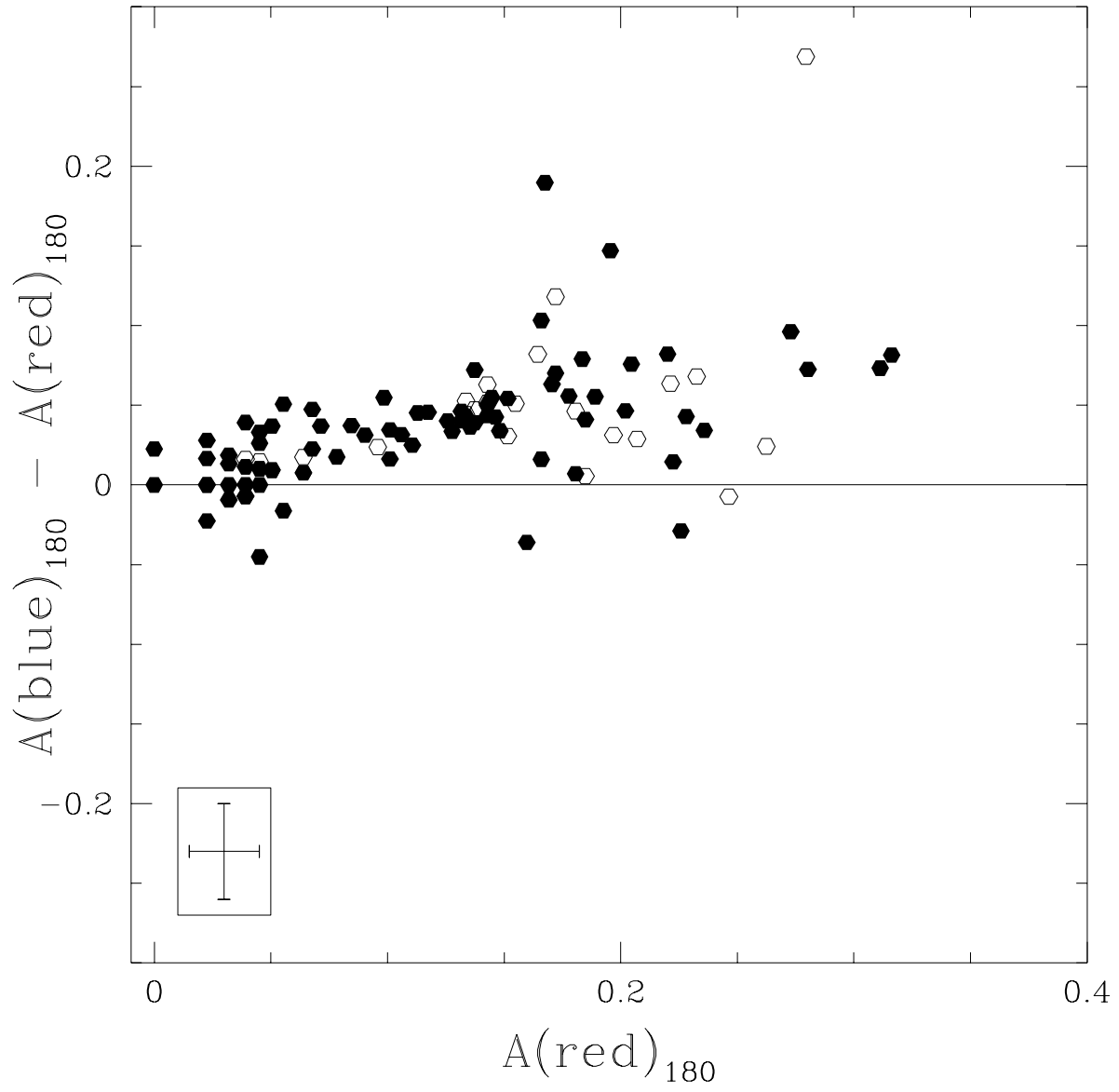


Fig. 2.—

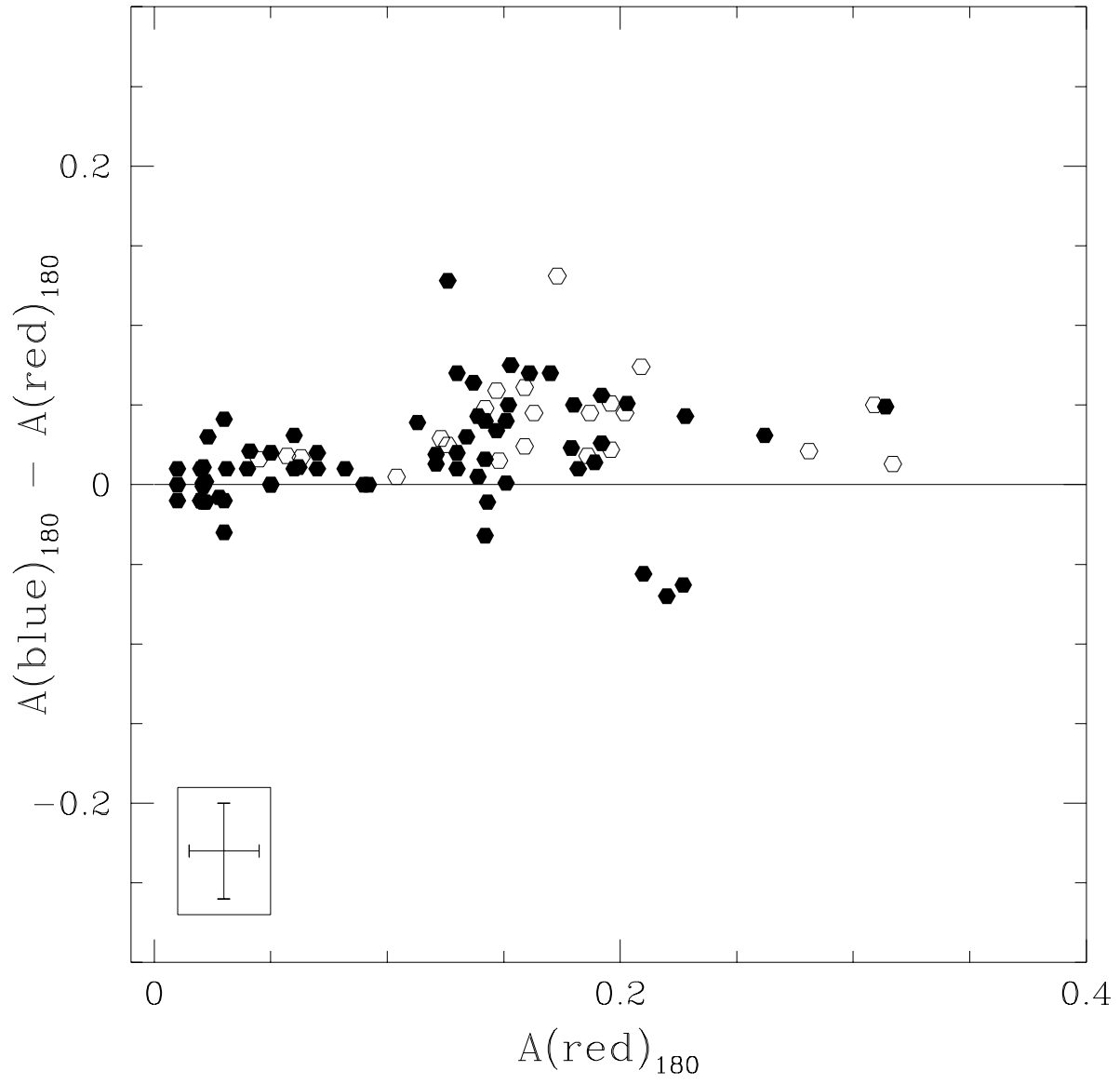


Fig. 3.—

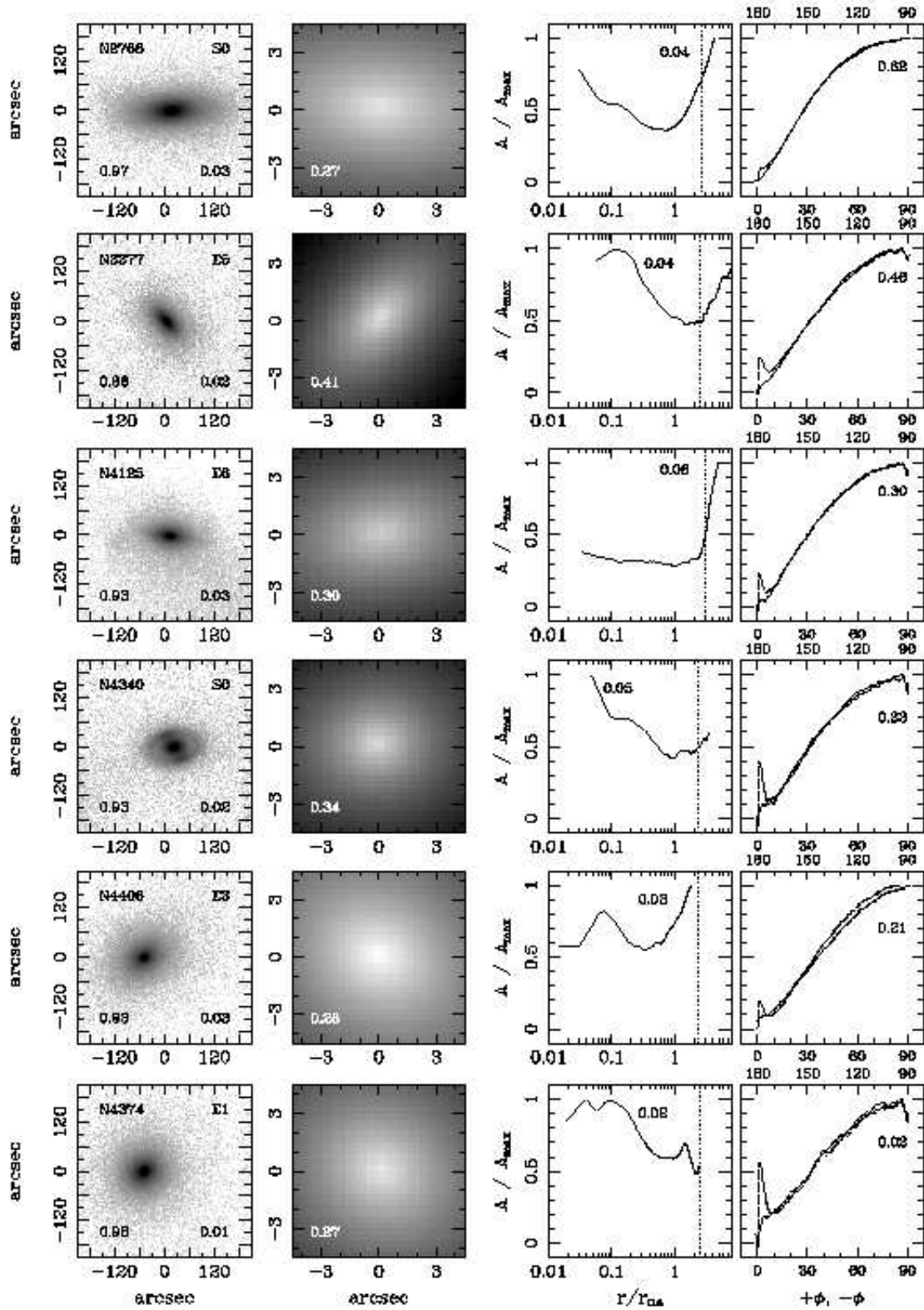


Fig. 4.—



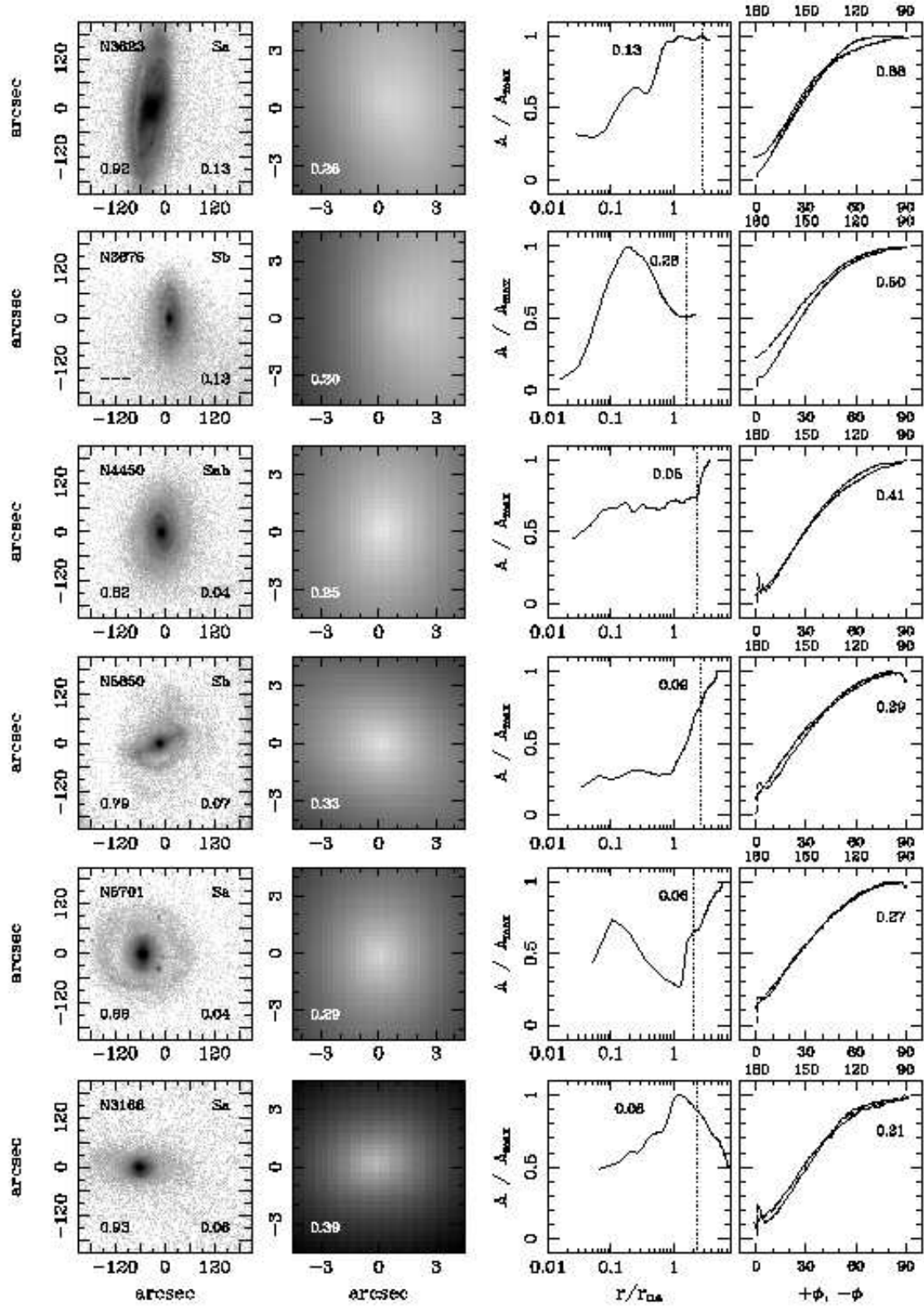


Fig. 5.—

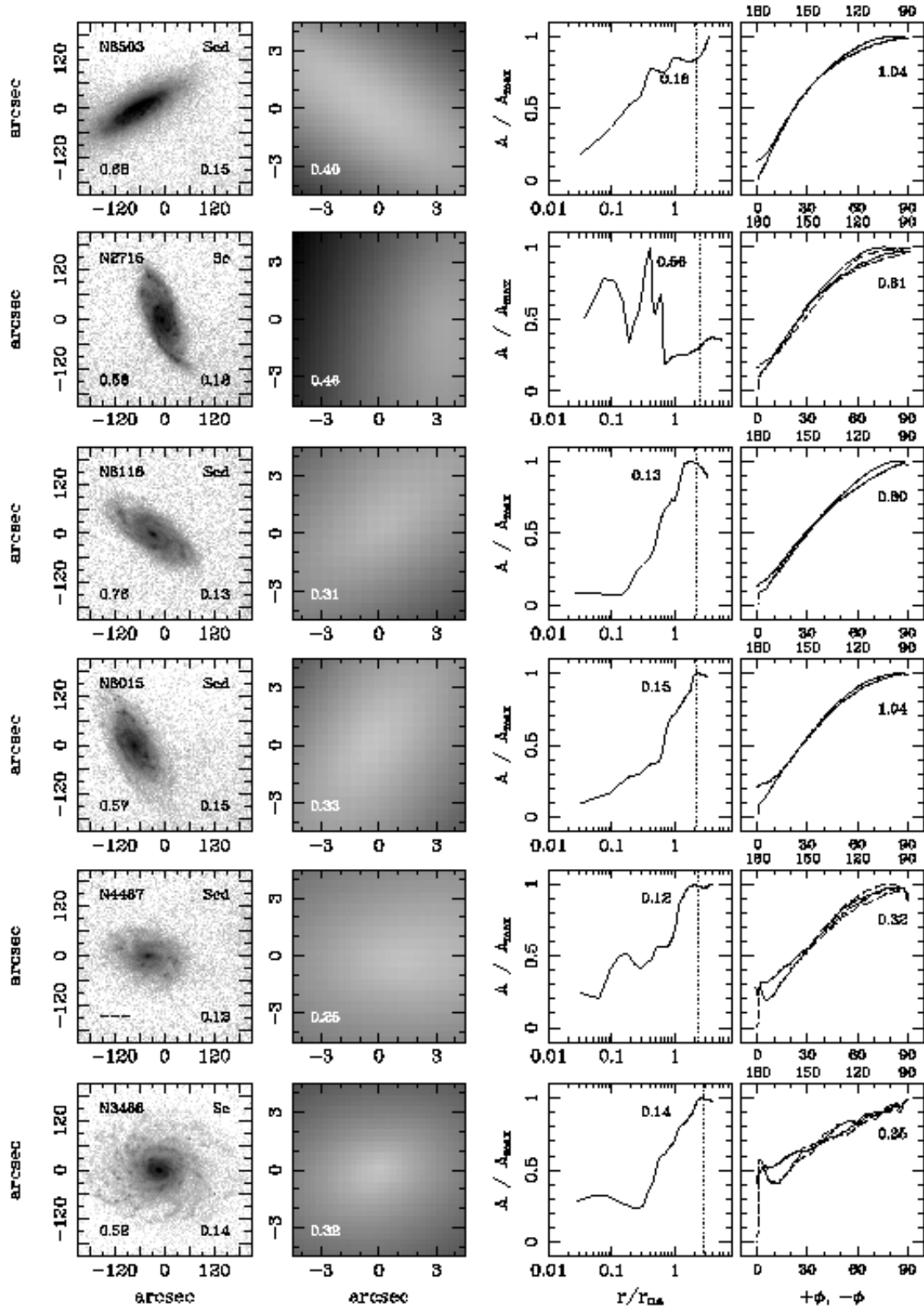


Fig. 6.—

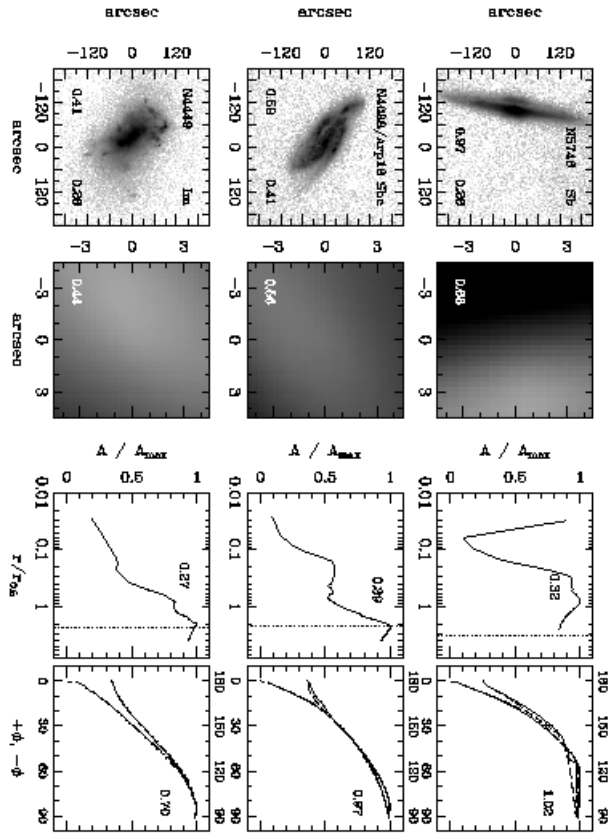


Fig. 7.—

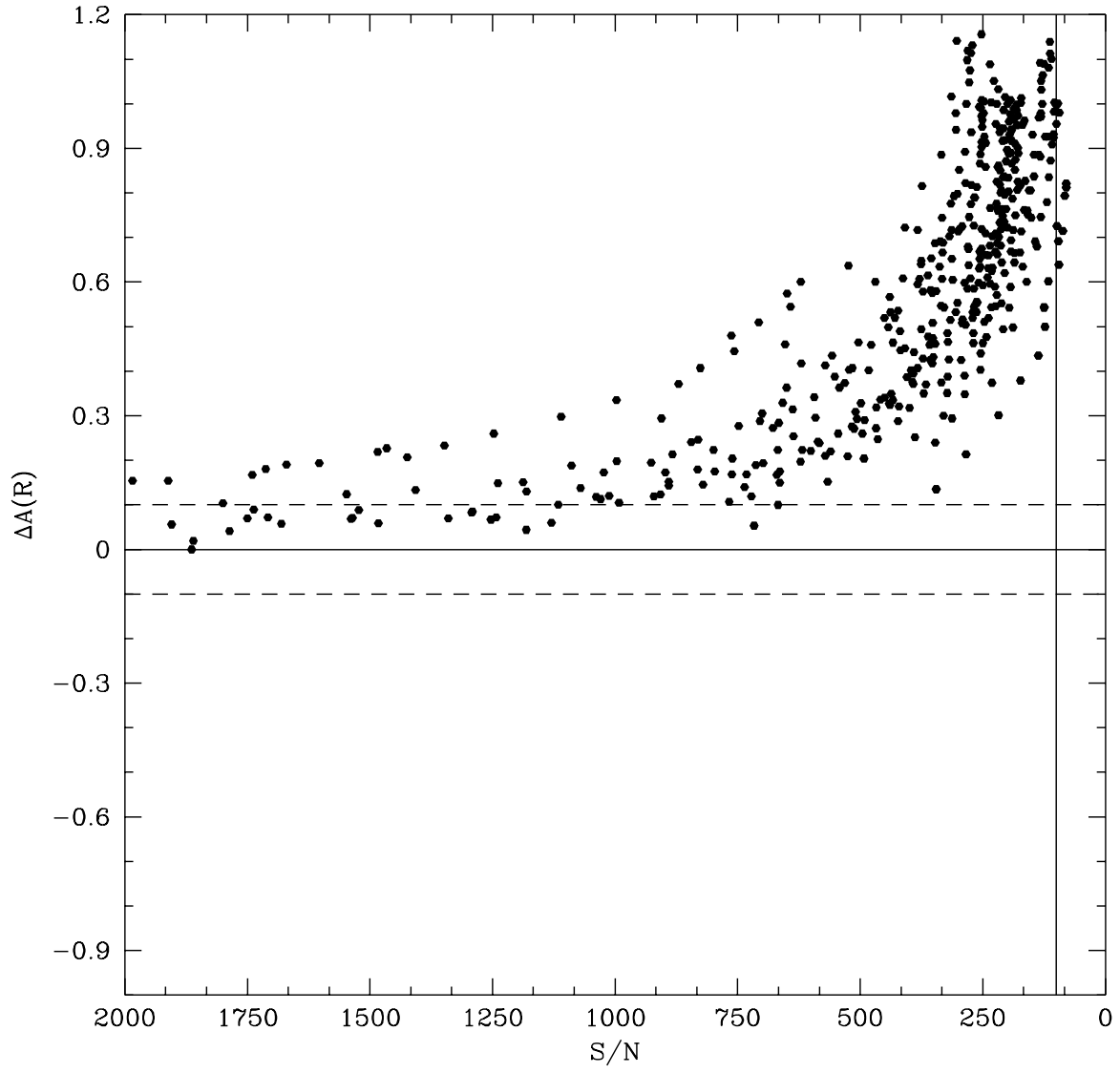


Fig. 8.—

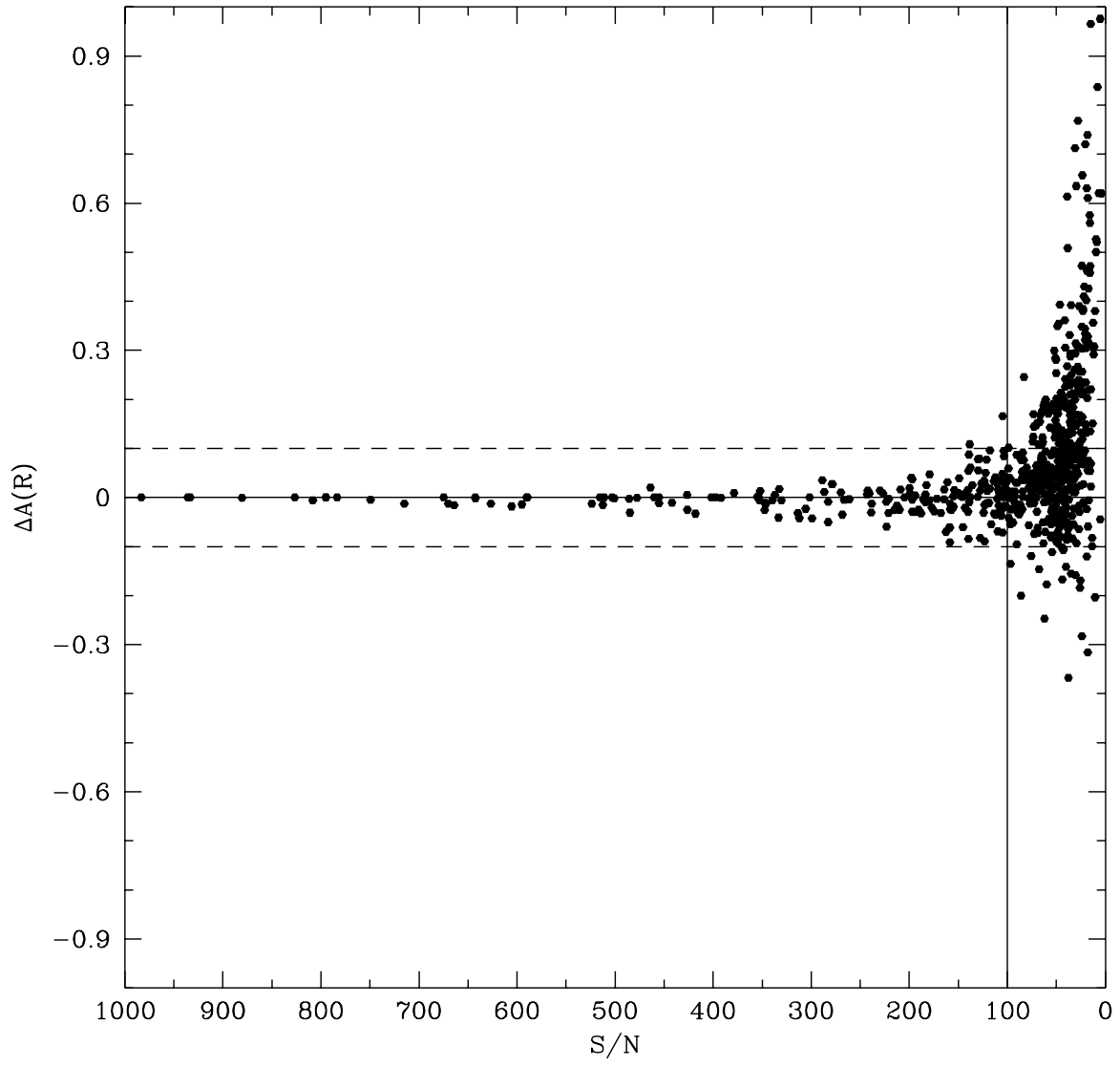


Fig. 9.—

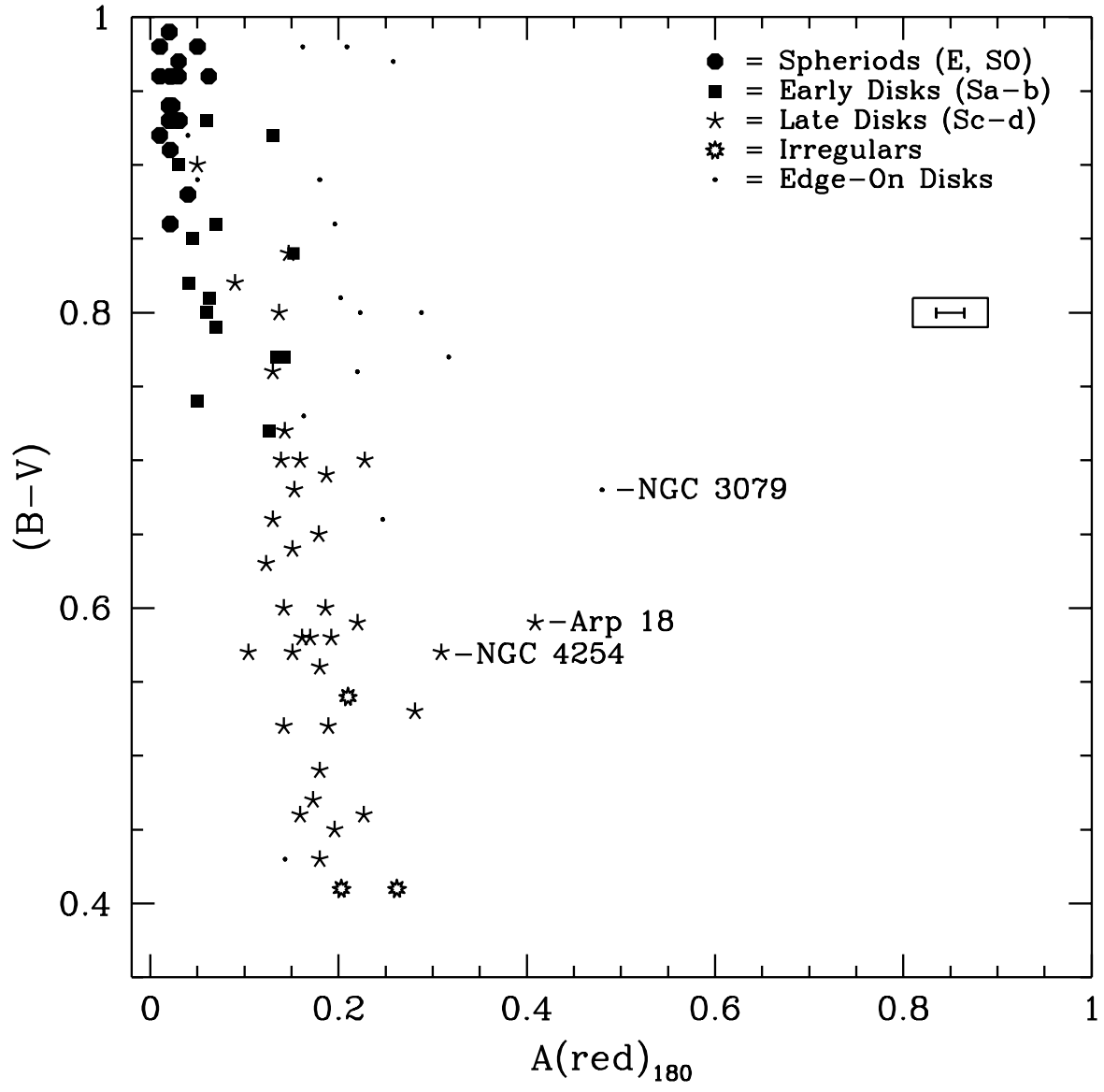


Fig. 10.—

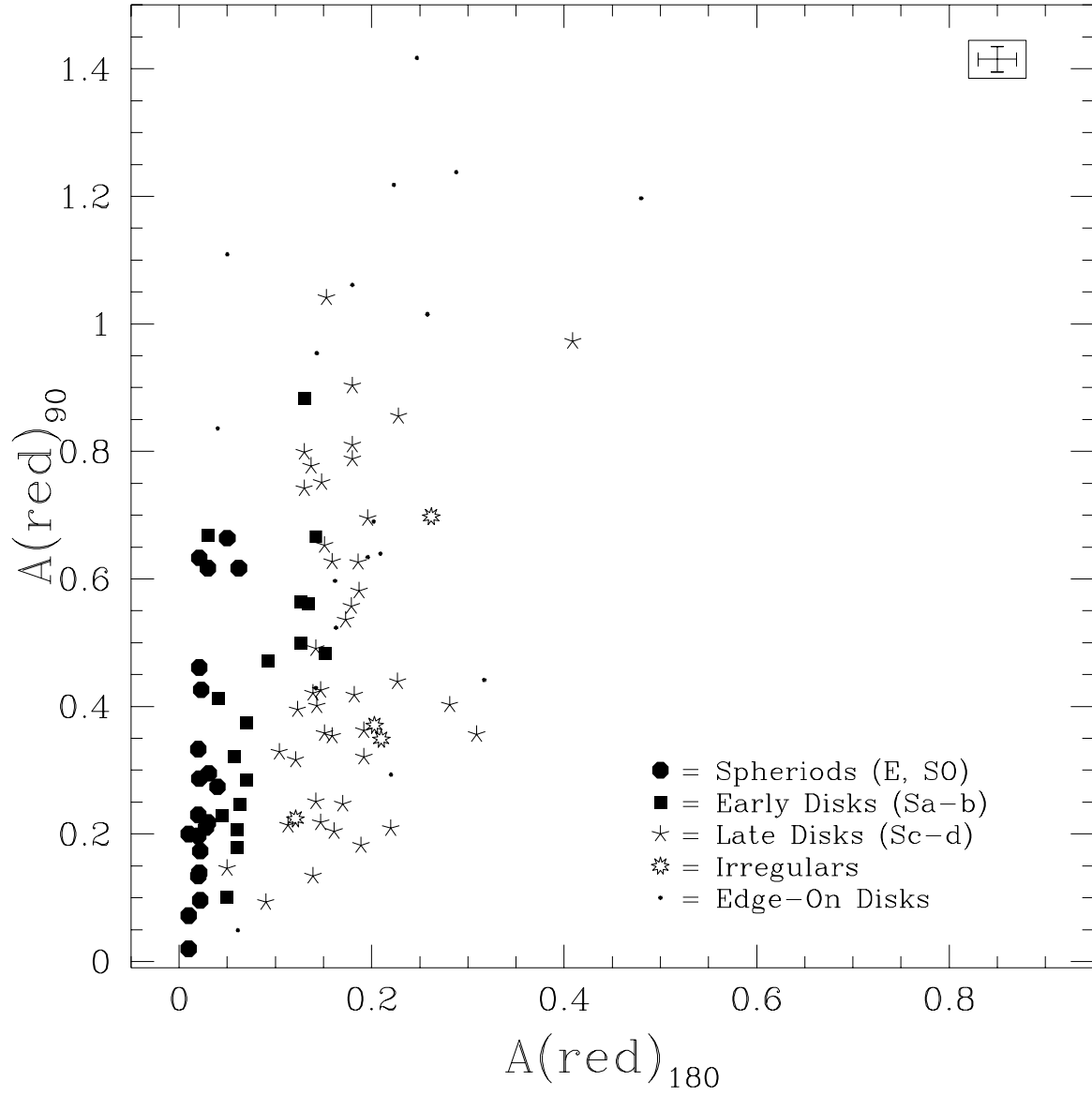


Fig. 11.—

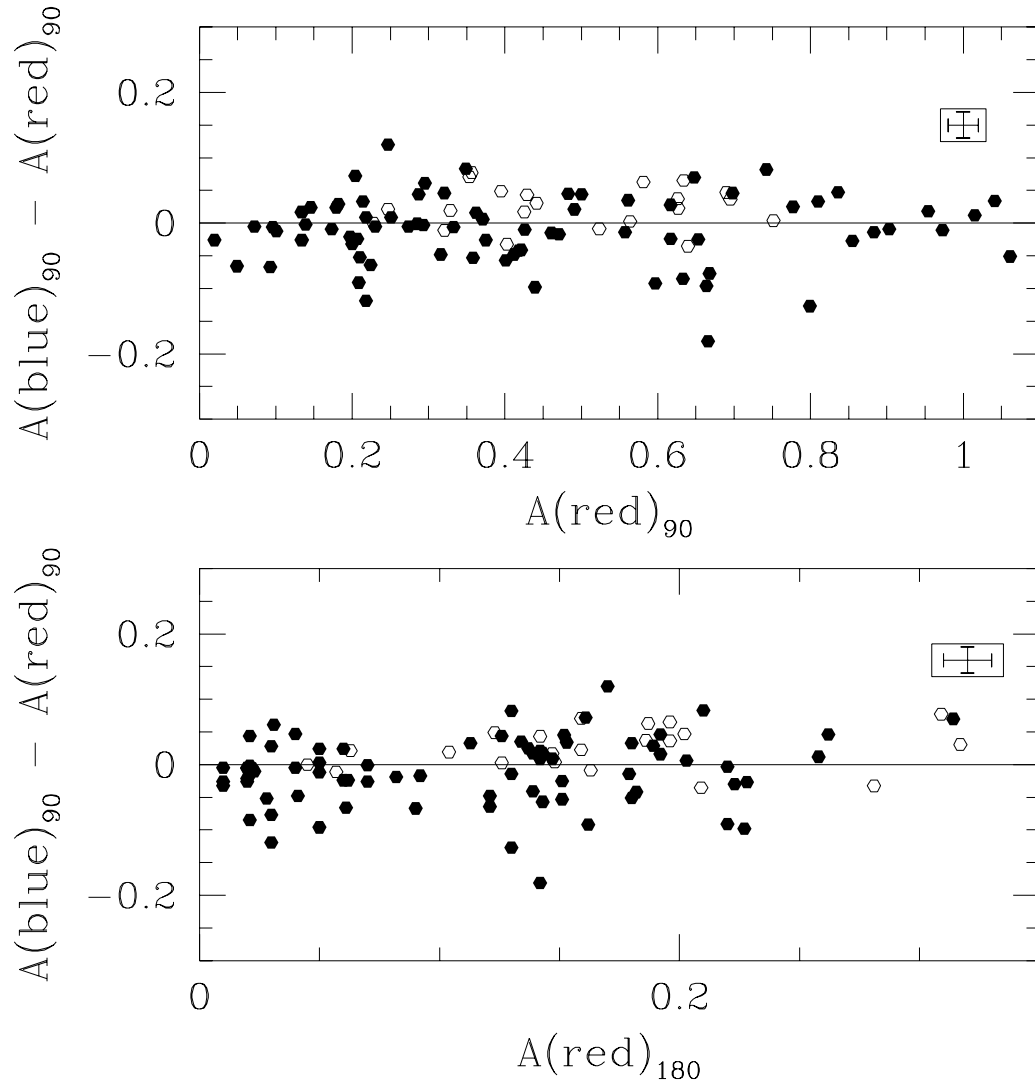


Fig. 12.—



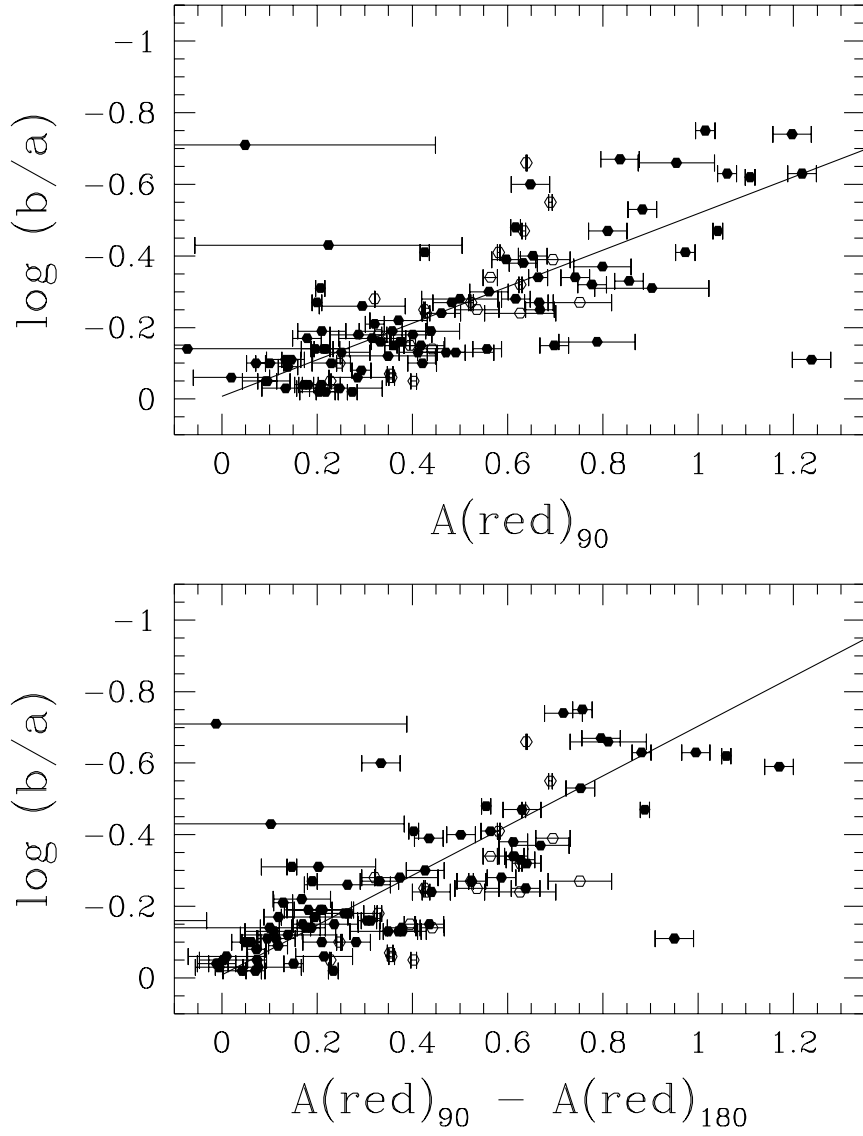


Fig. 13.—

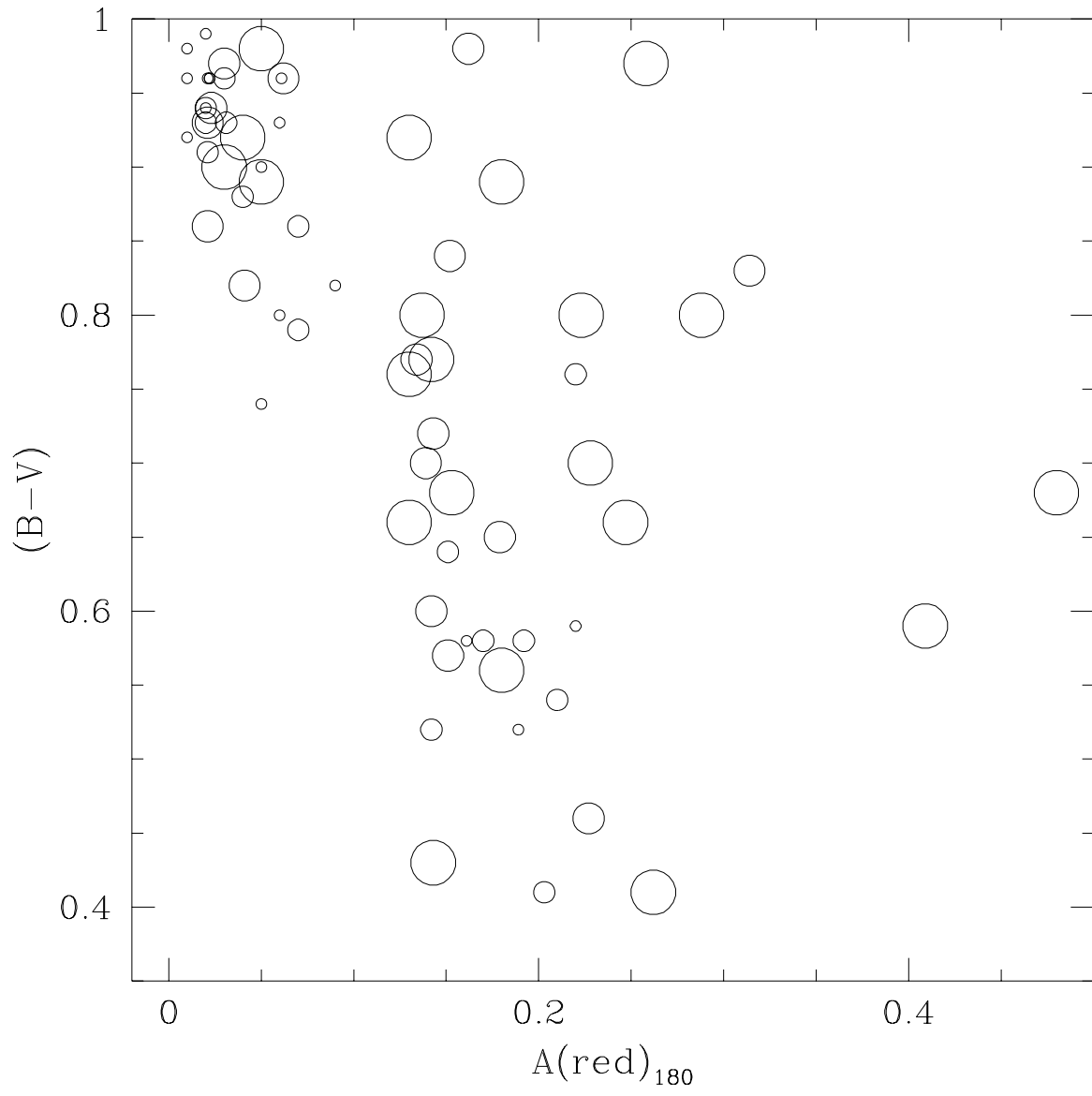


Fig. 14.—

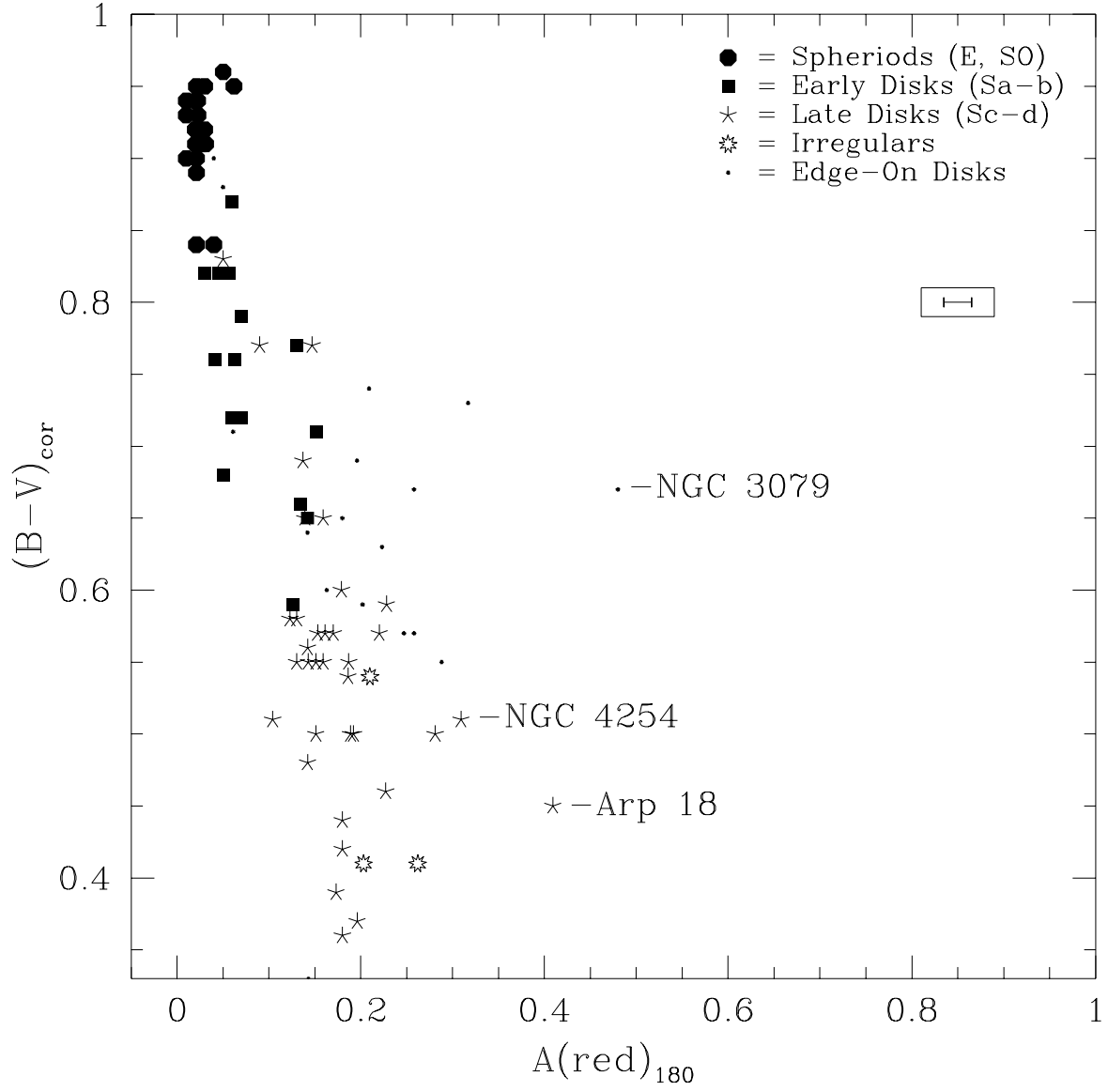


Fig. 15.—

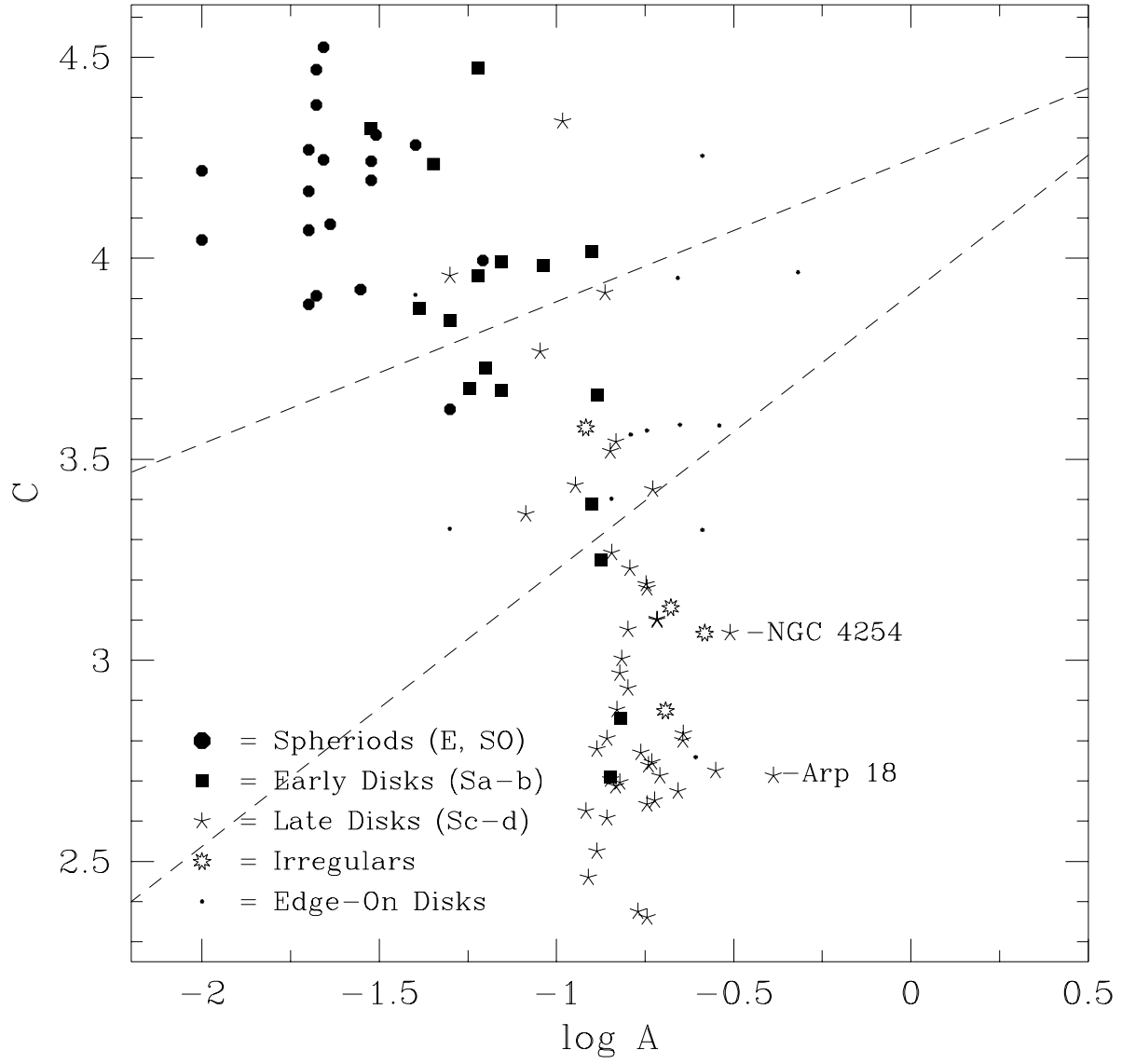


Fig. 16.—

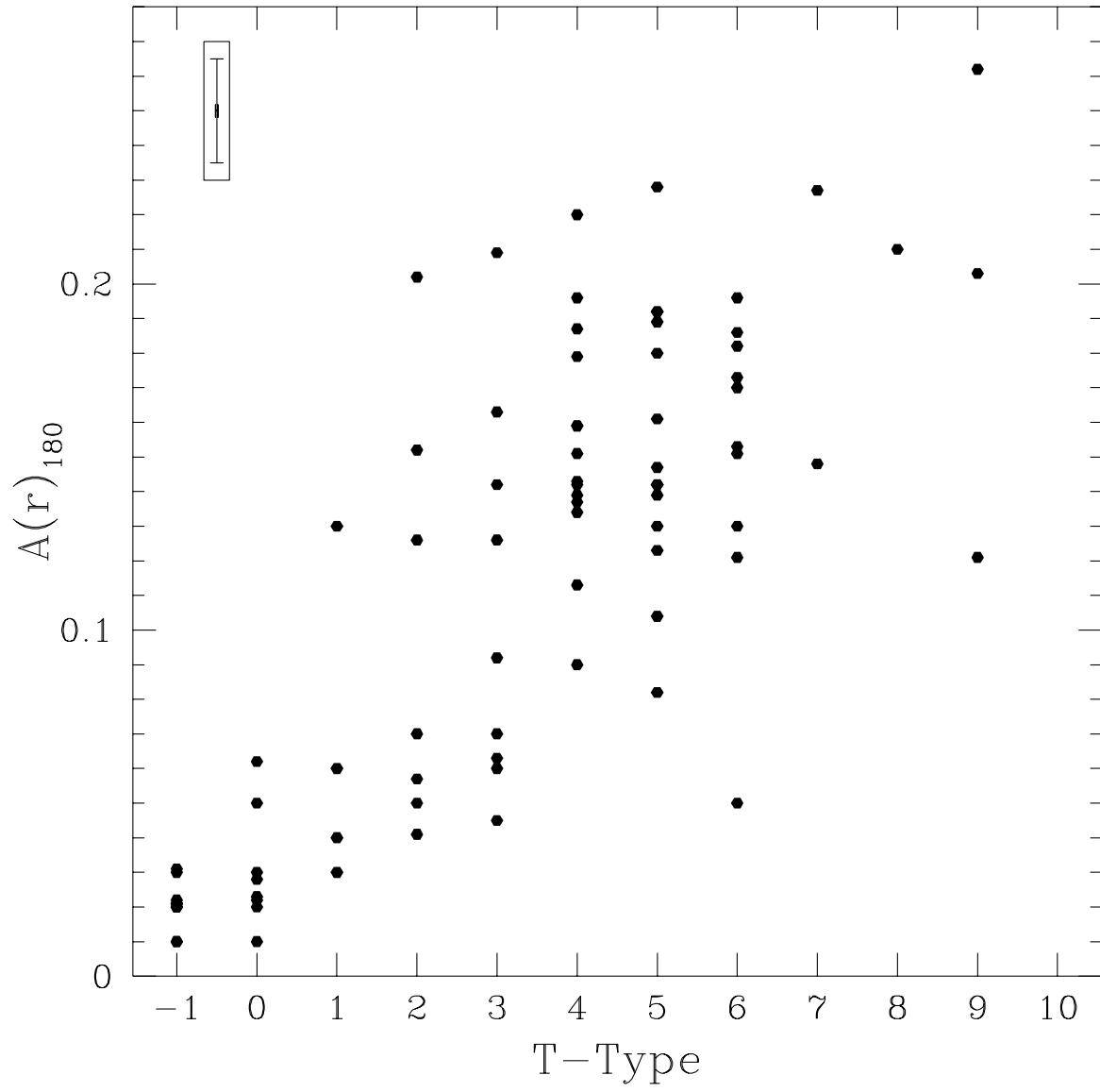


Fig. 17.—

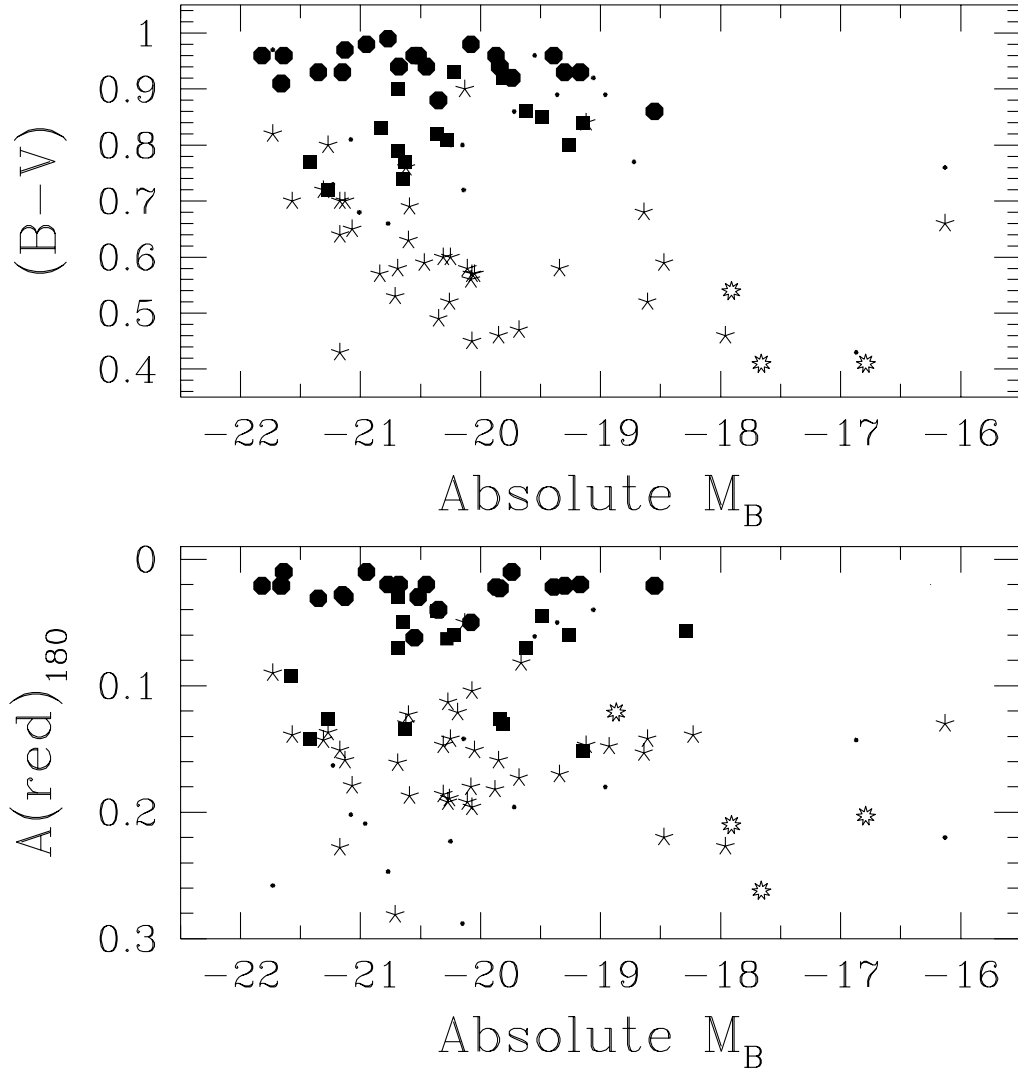


Fig. 18.—

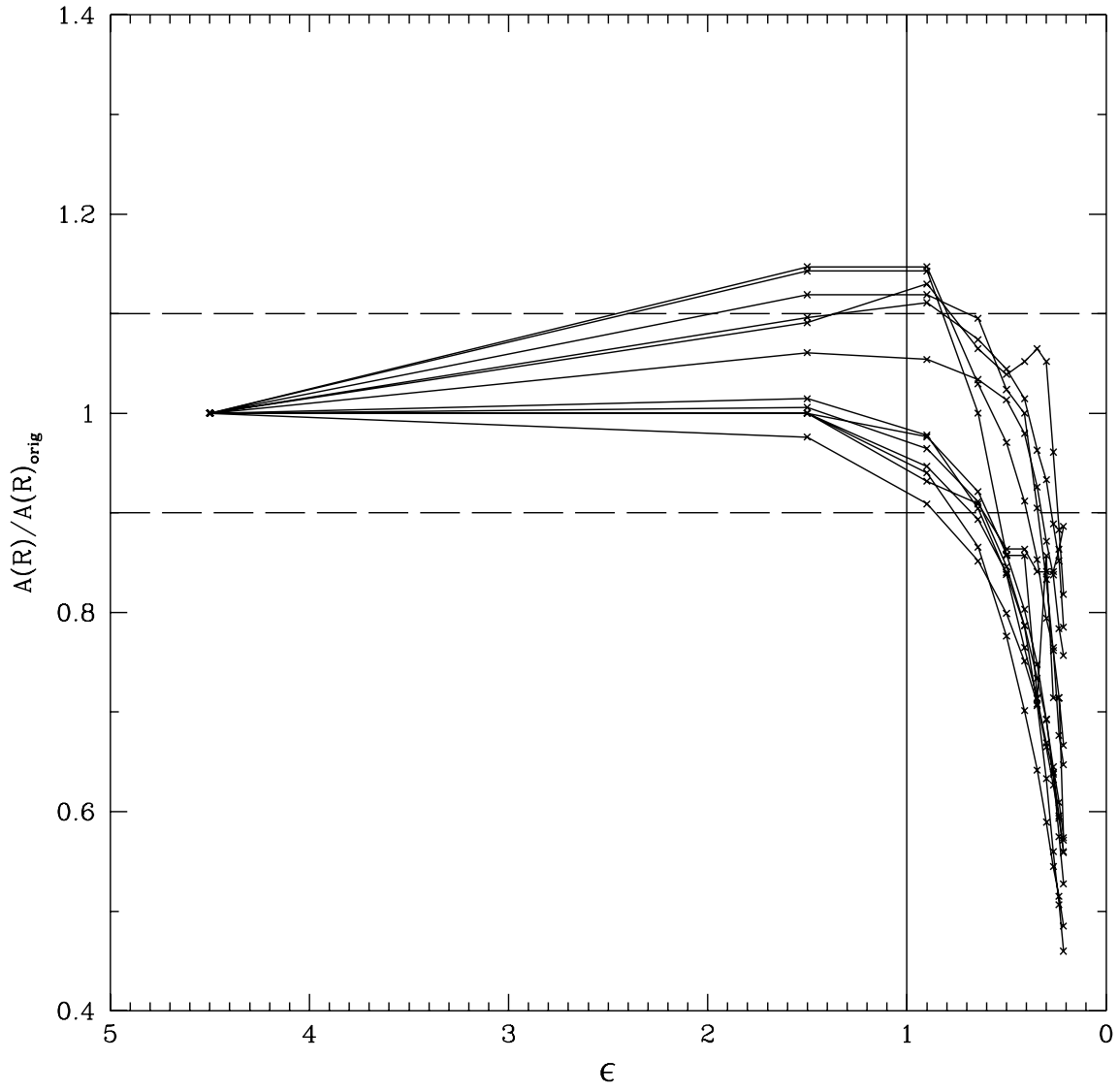


Fig. 19.—

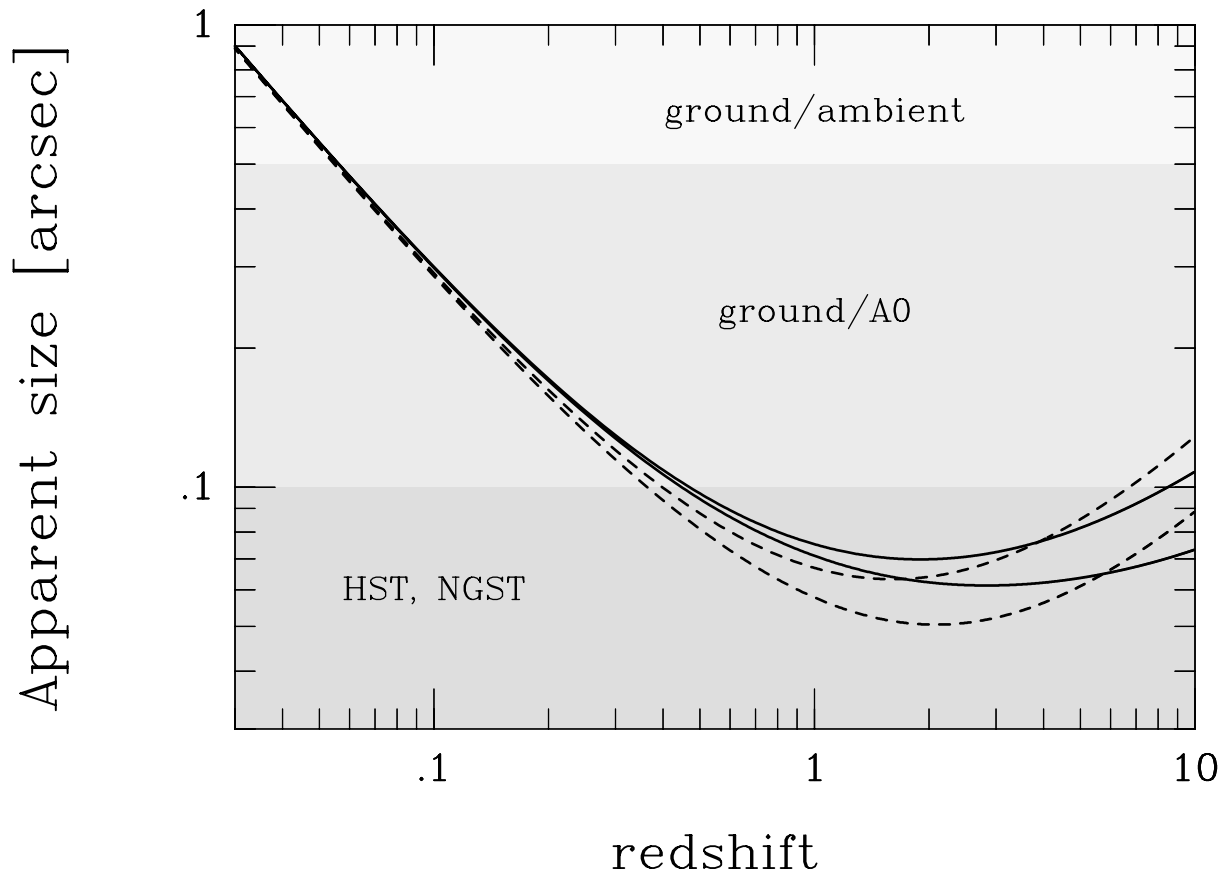


Fig. 20.—